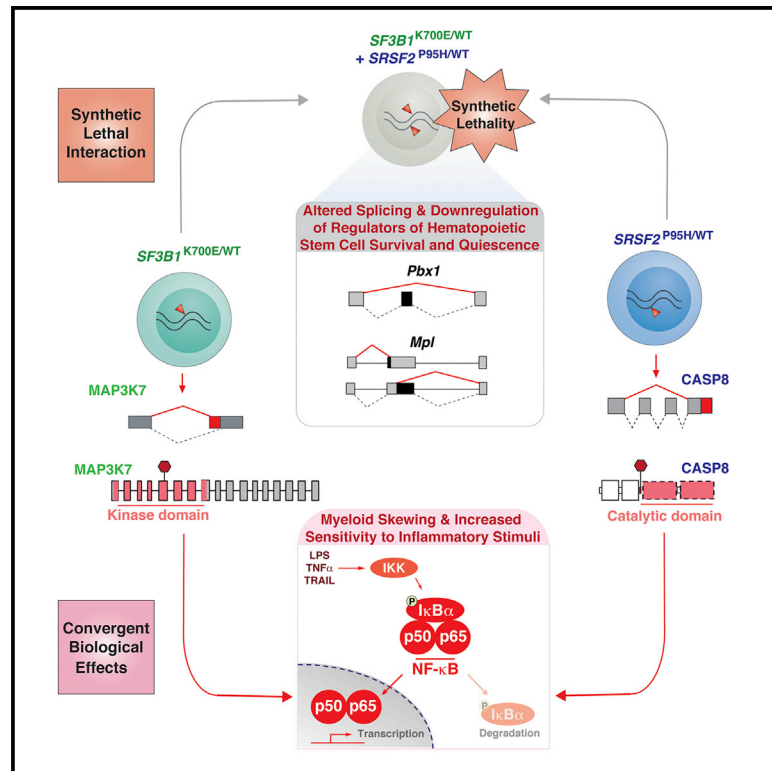


Synthetic Lethal and Convergent Biological Effects of Cancer-Associated Spliceosomal Gene Mutations

Graphical Abstract



Authors

Stanley Chun-Wei Lee,
Khrystyna North, Eunhee Kim, ...,
Benjamin L. Ebert, Robert K. Bradley,
Omar Abdel-Wahab

Correspondence

rbradley@fredhutch.org (R.K.B.),
abdelwao@mskcc.org (O.A.-W.)

In Brief

Lee et al. report that *SF3B1* and *SRSF2* mutations elicit distinct effects on splicing and are synthetically lethal due to the cumulative impact on hematopoietic stem cell survival and quiescence. These mutations share convergent effects on promoting NF- κ B signaling to drive myelodysplastic syndrome.

Highlights

- Mutations in *SF3B1* and *SRSF2* have a synthetic lethal interaction
- Mutations in RNA splicing factors are not tolerated in a homozygous state
- Mutations in *SF3B1* and *SRSF2* have distinct effects on pre-mRNA splicing
- Both *SF3B1* and *SRSF2* mutations result in hyperactive NF- κ B signaling



Synthetic Lethal and Convergent Biological Effects of Cancer-Associated Spliceosomal Gene Mutations

Stanley Chun-Wei Lee,^{1,11} Khrystyna North,^{2,3,4,11} Eunhee Kim,^{5,11} Eunjung Jang,⁵ Esther Obeng,^{6,10} Sydney X. Lu,¹ Bo Liu,¹ Daichi Inoue,¹ Akihide Yoshimi,¹ Michelle Ki,¹ Mirae Yeo,⁵ Xiao Jing Zhang,¹ Min Kyung Kim,¹ Hana Cho,¹ Young Rock Chung,¹ Justin Taylor,¹ Benjamin H. Durham,¹ Young Joon Kim,¹ Alessandro Pastore,¹ Sebastien Monette,⁷ James Palacino,⁸ Michael Seiler,⁸ Silvia Buonamici,⁸ Peter G. Smith,⁸ Benjamin L. Ebert,^{6,10} Robert K. Bradley,^{2,3,4,11,*} and Omar Abdel-Wahab^{1,9,11,12,*}

¹Human Oncology and Pathogenesis Program, Memorial Sloan Kettering Cancer Center, Zuckerman 701, 408 East 69th Street, New York, NY 10065, USA

²Computational Biology Program, Public Health Sciences Division, Fred Hutchinson Cancer Research Center, 1100 Fairview Avenue North, Mailstop: M1-B514, Seattle, WA 98109-1024, USA

³Basic Sciences Division, Fred Hutchinson Cancer Research Center, Seattle, WA, USA

⁴Department of Genome Sciences, University of Washington, Seattle, WA, USA

⁵School of Life Sciences, Ulsan National Institute of Science and Technology, Ulsan, Republic of Korea

⁶Division of Hematology, Department of Medicine, Brigham and Women's Hospital, Harvard Medical School, Boston, MA, USA

⁷Laboratory of Comparative Pathology, Memorial Sloan Kettering Cancer Center, Weill Cornell Medicine, The Rockefeller University, New York, NY, USA

⁸H3 Biomedicine, Cambridge, MA, USA

⁹Leukemia Service, Department of Medicine, Memorial Sloan Kettering Cancer Center, New York, NY, USA

¹⁰Broad Institute of MIT and Harvard, Cambridge, MA, USA

¹¹These authors contributed equally

¹²Lead Contact

*Correspondence: rbradley@fredhutch.org (R.K.B.), abdelwao@mskcc.org (O.A.-W.)

<https://doi.org/10.1016/j.ccell.2018.07.003>

SUMMARY

Mutations affecting RNA splicing factors are the most common genetic alterations in myelodysplastic syndrome (MDS) patients and occur in a mutually exclusive manner. The basis for the mutual exclusivity of these mutations and how they contribute to MDS is not well understood. Here we report that although different spliceosome gene mutations impart distinct effects on splicing, they are negatively selected for when co-expressed due to aberrant splicing and downregulation of regulators of hematopoietic stem cell survival and quiescence. In addition to this synthetic lethal interaction, mutations in the splicing factors SF3B1 and SRSF2 share convergent effects on aberrant splicing of mRNAs that promote nuclear factor κ B signaling. These data identify shared consequences of splicing-factor mutations and the basis for their mutual exclusivity.

INTRODUCTION

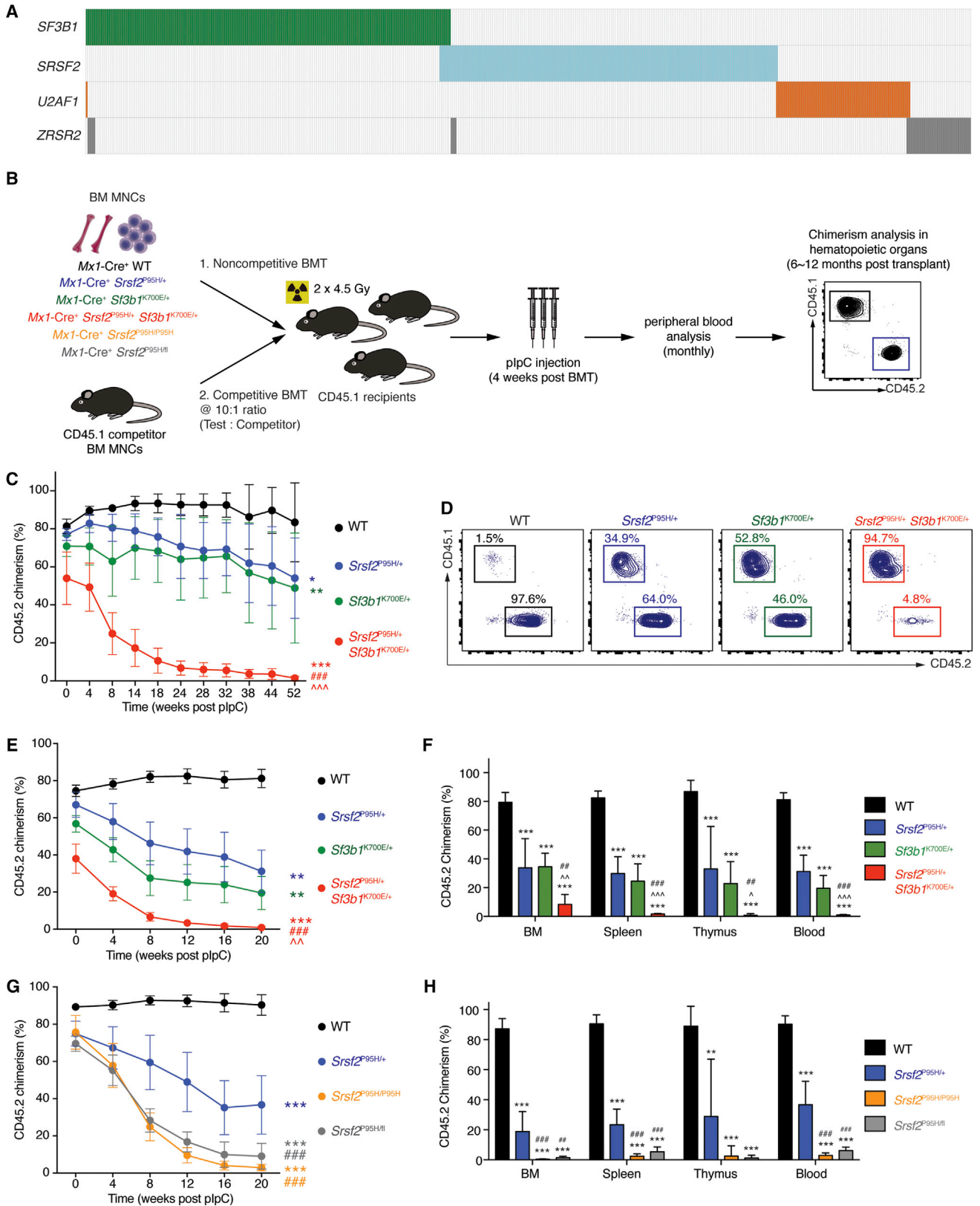
Recurrent mutations in genes encoding spliceosome components have been identified across multiple cancer types. Spliceosomal gene mutations most commonly occur in myelo-

dysplastic syndromes (MDS), chronic myelomonocytic leukemia (CMML), acute myeloid leukemia (AML) (Papaemmanuil et al., 2011; Yoshida et al., 2011), chronic lymphocytic leukemia (CLL) (Wang et al., 2011), and uveal melanoma (Harbour et al., 2013; Martin et al., 2013). SF3B1, U2AF1, and SRSF2 are the

Significance

Mutual exclusivity of different mutations that affect a single pathway in cancer is commonly thought to indicate convergent effects of these mutations. RNA splicing-factor mutations constitute the most common class of alterations in patients with myelodysplastic syndromes and are also frequent in several additional cancer types, and occur as heterozygous mutations at restricted residues in a mutually exclusive manner. The mutual exclusivity of spliceosomal mutations suggests synthetic lethal and/or convergent biological effects of these mutations; however, there is currently no functional evidence supporting either of these possibilities. Here we report that individual spliceosomal mutations have non-overlapping effects on splicing and are mutually exclusive due to both synthetic lethal interactions and convergent effects on hyperactivation of innate immune signaling.





(legend on next page)

most commonly mutated genes. Mutations in each of these occur as heterozygous point mutations at specific residues, suggesting gain-of-function alterations. In addition, mutations in spliceosome genes are mutually exclusive with one another, presumably due to redundant effects and/or a limit on cellular tolerance of disrupted spliceosome function.

Despite insights into the effects of each mutation on pre-mRNA splicing, the basis for their mutual exclusivity, and functionally convergent effects they may have are unknown. For example, recent work identified that mutations affecting the core splicing factor SF3B1 are associated with cryptic 3' splice site selection and altered branchpoint recognition (Darman et al., 2015; DeBoever et al., 2015). In contrast, mutations affecting SRSF2, an auxiliary splicing factor that binds exonic splicing enhancers to promote splicing, alter its RNA binding preference in a sequence-specific manner and thereby alter the efficiency of exon inclusion (Kim et al., 2015; Zhang et al., 2015). Finally, mutations affecting U2AF1 either promote or repress 3' splice site based on sequences flanking the AG dinucleotide (Ilagan et al., 2014). Given that the effects of SF3B1, U2AF1, and SRSF2 mutations on splicing mechanisms are distinct, it is unclear why these mutations are mutually exclusive. Moreover, evaluation of the effects of these mutations on splicing and gene expression in an isogenic manner has not been performed. Here we directly assessed the functional basis for the mutual exclusivity of spliceosome gene mutations using models expressing single- or double-mutant splicing factors simultaneously. These data provide a functional explanation for the genetic configuration of spliceosome gene mutations and identify a convergent effect of these mutations on a pathway of established relevance to MDS pathogenesis.

RESULTS

Simultaneous Expression of *Srsf2* and *Sf3b1* Mutations Is Incompatible with Hematopoiesis

Evaluation of sequencing data from >4,000 patients with myeloid neoplasms revealed that while ~48% (1,935/4,032) have a mutation in an RNA splicing factor, only ~2% of patients (86/4,032) have >1 splicing-factor mutation (Figure 1A and Table S1). To understand the basis of this mutual exclusivity,

we generated mice for inducible heterozygous expression of two of the most common splicing-factor mutations in MDS (*SF3B1*^{K700E} and *SRSF2*^{P95H}) simultaneously (Figure 1B). We performed noncompetitive bone marrow transplantation (BMT), whereby each mutation was induced following stable engraftment in recipient mice (Figure 1B). Bone marrow (BM) cells co-expressing *Srsf2*^{P95H} and *Sf3b1*^{K700E} mutations were severely defective in multi-lineage reconstitution compared with other groups (Figures 1C, 1D, and S1A–S1D). Chimerism analysis and evaluation for recombination prior to polyinosinic-polycytidylic acid (plpC) administration confirmed minimal spontaneous excision prior to BMT (Figures S1E and S1F). In competitive BMT (Figure 1E), BM cells co-expressing *Sf3b1*^{K700E} and *Srsf2*^{P95H} mutations were more readily outcompeted by competitor BM cells relative to single-mutant or wild-type (WT) controls. Analyses of hematopoietic organs 6 months post BMT revealed a near-complete absence of *Srsf2*^{P95H/+} *Sf3b1*^{K700E/+} cells, which was distinct from single-mutant groups (Figures 1E, 1F, and S1C). These data provide functional evidence that co-expression of mutant RNA splicing factors is not tolerated.

Expression of Splicing-Factor Mutations in a Homozygous or Hemizygous State Is Incompatible with Hematopoiesis

Prior studies identified that cells bearing mutant splicing factors require the WT allele for survival (Lee et al., 2016; Zhou et al., 2015). While these observations potentially explain the heterozygous nature of splicing-factor mutations in patients, the effect of expressing splicing-factor mutation in a homozygous manner was not assessed. To test this, we generated mice with conditional homozygous expression of the *SRSF2*^{P95H} mutation (*Mx1-Cre*⁺ *Srsf2*^{P95H/P95H}). In competitive BMT assays, hematopoietic stem and progenitor cells (HSPCs) from these mice showed severe defects in multi-lineage reconstitution relative to *Mx1-Cre*⁺ *Srsf2*^{P95H/+} or *Mx1-Cre*⁺ WT HSPCs, similar to defects seen with hemizygous *Srsf2*^{P95H} expression (*Mx1-Cre*⁺ *Srsf2*^{P95H/fl}) (Figures 1G, 1H, and S1G–S1I). These data firmly establish that neither hemizygous nor homozygous expression of splicing-factor mutations is tolerated, highlighting the unique dependency of spliceosome-mutant cells on residual WT spliceosome function.

Figure 1. Simultaneous Expression of Mutations in *Srsf2* and *Sf3b1* or Expression in the Homozygous State Is Incompatible with Hematopoiesis

(A) Heatmap of the four most commonly mutated genes encoding RNA splicing factors across 11 studies in myeloid malignancies (Bejar et al., 2012; Damm et al., 2012; Haferlach et al., 2014; Lasho et al., 2012; Makishima et al., 2012; Meggendorfer et al., 2012; Papaemmanuil et al., 2013; Patnaik et al., 2013; Thol et al., 2012; Yoshida et al., 2011; Zhang et al., 2012). Each column represents a patient, and each colored bar represents the presence of the specified mutation.

(B) Schema of competitive and noncompetitive bone marrow transplantation (BMT) using bone marrow mononuclear cells (BM MNCs) from 8-week-old *Mx1-Cre*⁺ wild-type (WT), *Mx1-Cre*⁺ *Srsf2*^{P95H/+}, *Mx1-Cre*⁺ *Sf3b1*^{K700E/+}, *Mx1-Cre*⁺ *Srsf2*^{P95H/+} *Sf3b1*^{K700E/+}, *Mx1-Cre*⁺ *Srsf2*^{P95H/P95H}, and *Mx1-Cre*⁺ *Srsf2*^{P95H/fl} mice. Polyinosinic-polycytidylic acid (plpC) was administered to recipients 4 weeks post BMT to induce expression of mutant alleles.

(C) Percentage of CD45.2 chimerism in peripheral blood of recipients (n = 8–10 mice per genotype) in noncompetitive BMT.

(D) Representative fluorescence-activated cell sorting (FACS) plots of CD45.2⁺ cells in peripheral blood of recipients in noncompetitive BMT 52 weeks post plpC.

(E) Percentage of CD45.2 chimerism in peripheral blood of recipients (n = 10 mice per genotype) in competitive BMT.

(F) Analysis of CD45.2 chimerism in the BM, spleen, thymus, and blood of recipients (n = 5–10 mice per genotype) in competitive BMT 20 weeks post plpC.

(G) Percentage of CD45.2 chimerism in peripheral blood of recipients (n = 5–10 mice per genotype) in competitive BMT from *Mx1-Cre*⁺ WT, *Mx1-Cre*⁺ *Srsf2*^{P95H/+}, *Mx1-Cre*⁺ *Srsf2*^{P95H/P95H}, and *Mx1-Cre*⁺ *Srsf2*^{P95H/fl} mice.

(H) Analysis of CD45.2 chimerism in BM, spleen, thymus, and blood of recipients (n = 5–10 mice per genotype) in competitive BMT 20 weeks post plpC. Error bars represent mean ± SD. ANOVA and Tukey's post hoc test were used to compare groups. *p < 0.05, **p < 0.01, ***p < 0.001 versus *Mx1-Cre*⁺ WT mice; ^p < 0.05, ^^p < 0.01, ^^p < 0.001 versus *Mx1-Cre*⁺ *Sf3b1*^{K700E/+} mice; ##p < 0.01, ###p < 0.001 versus *Mx1-Cre*⁺ *Srsf2*^{P95H/+} mice. See also Figure S1 and Table S1.

Simultaneous Expression of *Srsf2* and *Sf3b1* Mutations Resulted in Increased Apoptosis and Reduced Quiescence of HSPCs

To identify why co-expression of *Srsf2*^{P95H} and *Sf3b1*^{K700E} resulted in severe HSPC dysfunction, we performed cell-cycle and apoptosis analysis. Two-weeks following recombination, there was a significant increase in lineage⁻ Sca-1⁺ c-Kit⁺ (LSK) cells undergoing apoptosis and in the S phase of cell cycle in *Mx1-Cre*⁺ *Srsf2*^{P95H/+} *Sf3b1*^{K700E/+} mice relative to controls (Figures 2A and 2B).

Selection against co-expression of two mutant splicing factors was strongly supported by the fact that mice with hematopoietic-specific expression of *Srsf2*^{P95H} and *Sf3b1*^{K700E} (*Vav-Cre*⁺ *Srsf2*^{P95H/+} *Sf3b1*^{K700E/+}) mutations were associated with 100% lethality at weaning, while single-mutant mice were present at the expected frequencies (Figure 2C). Analysis of 139 embryos at embryonic day 14.5 (E14.5) revealed that *Vav-Cre*⁺ *Srsf2*^{P95H/+} *Sf3b1*^{K700E/+} fetuses were detectable at the expected frequency (Figures S2A and S2B). E14.5 *Vav-Cre*⁺ *Srsf2*^{P95H/+} *Sf3b1*^{K700E/+} fetal livers had increased number of LSK cells as well as phenotypic long-term hematopoietic stem cell (LT-HSC, LSK CD150⁺ CD48⁻), multi-potent progenitor (MPP, LSK CD150⁻ CD48⁻), HPC-1 (LSK CD150⁻ CD48⁺), and HPC-2 (LSK CD150⁺ CD48⁺) populations compared with all other genotypes (Figures 2D, 2E, and S2C–S2G). Despite a significant increase in HSPCs, *Vav-Cre*⁺ *Srsf2*^{P95H/+} *Sf3b1*^{K700E/+} fetal liver cells had significantly impaired colony-forming ability *in vitro* (Figure 2F) and markedly increased percentage of cycling and apoptotic cells (Figures 2G–2I). These derangements in HSPC phenotypes were manifest by E18.5 when *Vav-Cre*⁺ *Srsf2*^{P95H/+} *Sf3b1*^{K700E/+} fetuses had near absence of hematopoietic cells in the BM as well as increased apoptotic cells in fetal liver (Figures S2H and S2I). Taken together, these data demonstrate that co-expression of splicing-factor mutations compromises hematopoiesis, driven by aberrant cell-cycle progression and increased apoptosis of HSPCs.

Srsf2 and *Sf3b1* Mutations Have Largely Distinct Effects on Gene Expression

To understand the mechanistic basis for mutual exclusivity of *SF3B1* and *SRSF2* mutations, we performed RNA sequencing (RNA-seq) on lineage⁻ c-Kit⁺ (LK) cells from *Mx1-Cre*⁺ *Srsf2*^{P95H/+} *Sf3b1*^{K700E/+} mice as well as single-mutant and WT controls (Figure 3A). The mean allelic ratio of *Sf3b1*^{K700E} and *Srsf2*^{P95H} expressed in double-mutant cells was 20.7% and 33.5%, markedly lower than the ~50% expression in single-mutant controls, illustrating the intolerance of combining *SF3B1* and *SRSF2* mutations (Figure 3B). Expression of either mutation resulted in dysregulation of hundreds of coding genes (Figure 3C and Table S2). *Mx1-Cre*⁺ *Srsf2*^{P95H/+} *Sf3b1*^{K700E/+} cells exhibited significantly more gene dysregulation than single-mutant cells, consistent with their more dramatic biological phenotype (Figure 3D). Double-mutant cells shared a greater proportion of differentially expressed genes with each single-mutant group than single mutants shared with one another (Figure 3E). Gene ontology (GO) analysis of coding genes differentially expressed within each genotype relative to WT control revealed strong signatures of impaired hematopoiesis in dou-

ble-mutant cells, consistent with the multi-lineage defects in these cells (Figure 3F and Table S3).

We next tested whether mutations in *SF3B1* and *SRSF2* have independent effects on gene expression: that is, whether double-mutant cells recapitulated the gene dysregulation observed for each single-mutant genotype relative to WT. Approximately 80% and 40% of genes dysregulated in *Mx1-Cre*⁺ *Sf3b1*^{K700E/+} and *Mx1-Cre*⁺ *Srsf2*^{P95H/+} single-mutant cells were also dysregulated in *Mx1-Cre*⁺ *Sf3b1*^{K700E/+} *Srsf2*^{P95H/+} double-mutant cells (Figure 3E and Table S2). That degree of recapitulation of gene dysregulation was highly similar to and statistically indistinguishable ($p = 0.90$ and 0.44 for *Sf3b1*^{K700E} and *Srsf2*^{P95H} mutations, respectively) from expected recapitulation under the assumption of independence (Figure S3A). We therefore conclude that *SF3B1* and *SRSF2* mutations have independent effects on gene expression even when present in the same cell. Interestingly, in addition to recapitulating the dysregulation of specific genes expected based on single-mutant cells, double-mutant cells exhibited additional gene dysregulation (Figures S3B and S3C), consistent with the severe hematopoietic phenotype of these cells. These results suggest that *SF3B1* and *SRSF2* mutations have independent but compound effects on gene expression when present in the same cell.

Srsf2 and *Sf3b1* Mutations Have Distinct and Independent Effects on Splicing

We next assessed the consequences of single versus double mutations in *Sf3b1* and *Srsf2* on splicing (Table S4). Mutations in *SF3B1* have been proposed to alter 3' splice site recognition (Darman et al., 2015; DeBoever et al., 2015). In contrast, mutations in *SRSF2* alter exon recognition via preferential recognition of C-rich exonic splicing enhancer (ESE) motifs relative to G-rich ESEs, while WT *SRSF2* recognizes both classes of ESEs (Kim et al., 2015; Zhang et al., 2015). Our current understanding of *SF3B1* and *SRSF2* mutations therefore indicates that they induce distinct changes in splicing. However, the consequences of these mutations on splicing have not been compared in an isogenic context.

We used our double-mutant system to directly compare the effects of *SF3B1* and *SRSF2* mutations on RNA splicing. Consistent with prior studies, *Sf3b1* and *Srsf2* mutations affected 3' splice site and exon recognition, respectively (Figures 4A, 4B, S4A, and S4B). We observed a modest enrichment of adenosines upstream of intron-proximal 3' splice site promoted by the *Sf3b1*^{K700E} mutation, independent of the *Srsf2*^{P95H} mutation (Figure S4C). This enrichment was absent from cells expressing *Srsf2*^{P95H} alone. Cassette exons promoted versus repressed in cells expressing *Srsf2*^{P95H} were respectively enriched for CCNG and GGNG ESEs, independent of the presence or absence of *Sf3b1*^{K700E}, but were absent from cells expressing *Sf3b1*^{K700E} alone (Figures 4C and S4D). These analyses are consistent with previous reports that *SF3B1* and *SRSF2* mutations affect branchpoint recognition and ESE preference, respectively, and further demonstrate that these changes in splicing are specific to *SF3B1* and *SRSF2* mutations.

As *Sf3b1* and *Srsf2* mutations cause distinct changes in splicing, even when simultaneously present, we hypothesized that the effects of these mutations on splicing were independent. Consistent with this hypothesis, double-mutant cells

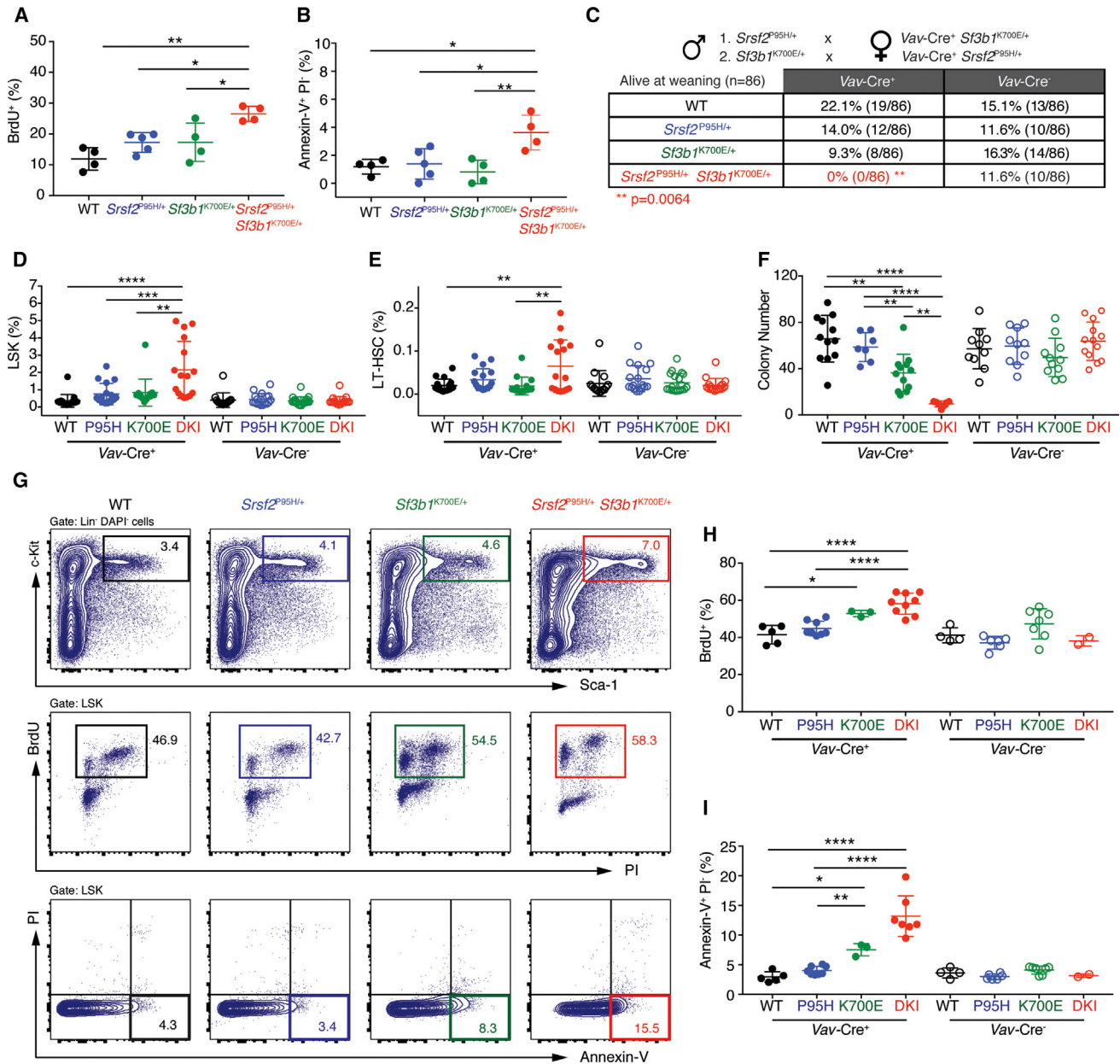


Figure 2. Combined Expression of Mutations in *Srsf2* and *Sf3b1* Results in Hematopoietic Stem and Progenitor Cell Apoptosis and Loss of Quiescence

(A and B) Percentage of bromodeoxyuridine⁺ (BrdU⁺) (A) or annexin-V⁺ propidium iodide⁻ (PI⁻) (B) LSK cells from *Mx1-Cre*⁺ WT (n = 4), *Mx1-Cre*⁺ *Srsf2*^{P95H/+} (n = 5), *Mx1-Cre*⁺ *Sf3b1*^{K700E/+} (n = 4), and *Mx1-Cre*⁺ *Srsf2*^{P95H/+} *Sf3b1*^{K700E/+} (n = 4) mice 2 weeks post plpC administration.

(C) Number of live mice at weaning from crossing *Sf3b1*^{K700E/+} mice to *Vav-Cre*⁺ *Srsf2*^{P95H/+} mice or by crossing *Srsf2*^{P95H/+} mice to *Vav-Cre*⁺ *Sf3b1*^{K700E/+} mice. **p = 0.0064; two-sided Chi-square test.

(D and E) Percentage of LSK (D) and long-term hematopoietic stem cells (LT-HSC; LSK CD150⁺ CD48⁻) (E) in E14.5 fetal livers from *Vav-Cre*⁺ WT (WT; n = 17), *Vav-Cre*⁺ *Srsf2*^{P95H/+} (P95H; n = 17), *Vav-Cre*⁺ *Sf3b1*^{K700E/+} (K700E; n = 15), and *Vav-Cre*⁺ *Srsf2*^{P95H/+} *Sf3b1*^{K700E/+} double-knockin (DKI; n = 16) fetuses and *Vav-Cre*⁻ WT (n = 14), *Vav-Cre*⁻ *Srsf2*^{P95H/+} (P95H; n = 17), *Vav-Cre*⁻ *Sf3b1*^{K700E/+} (K700E; n = 19), and *Vav-Cre*⁻ *Srsf2*^{P95H/+} *Sf3b1*^{K700E/+} DKI (n = 17) fetuses.

(F) Colony numbers from E14.5 fetal liver cells from *Vav-Cre*⁺ WT (n = 12), *Vav-Cre*⁺ *Srsf2*^{P95H/+} (P95H; n = 7), *Vav-Cre*⁺ *Sf3b1*^{K700E/+} (K700E; n = 12), and *Vav-Cre*⁺ *Srsf2*^{P95H/+} *Sf3b1*^{K700E/+} DKI (n = 7) fetuses and from *Vav-Cre*⁻ WT (n = 10), *Vav-Cre*⁻ *Srsf2*^{P95H/+} (P95H; n = 10), *Vav-Cre*⁻ *Sf3b1*^{K700E/+} (K700E; n = 11), and *Vav-Cre*⁻ *Srsf2*^{P95H/+} *Sf3b1*^{K700E/+} DKI (n = 13) fetuses.

(G–I) Representative FACS plots (G) and quantitation of BrdU⁺ (H) and annexin-V⁺ PI⁻ (I) LSK cells from *Vav-Cre*⁺ WT (n = 5), *Vav-Cre*⁺ *Srsf2*^{P95H/+} (P95H; n = 8), *Vav-Cre*⁺ *Sf3b1*^{K700E/+} (K700E; n = 3), and *Vav-Cre*⁺ *Srsf2*^{P95H/+} *Sf3b1*^{K700E/+} DKI (n = 9) fetuses and from *Vav-Cre*⁻ WT (n = 4), *Vav-Cre*⁻ *Srsf2*^{P95H/+} (P95H; n = 6), *Vav-Cre*⁻ *Sf3b1*^{K700E/+} (K700E; n = 7), and *Vav-Cre*⁻ *Srsf2*^{P95H/+} *Sf3b1*^{K700E/+} DKI (n = 2) fetuses.

Error bars represent mean ± SD. ANOVA and Tukey's post hoc test was used to compare groups. *p < 0.05, **p < 0.01, ***p < 0.001, ****p < 0.0001. See also Figure S2.

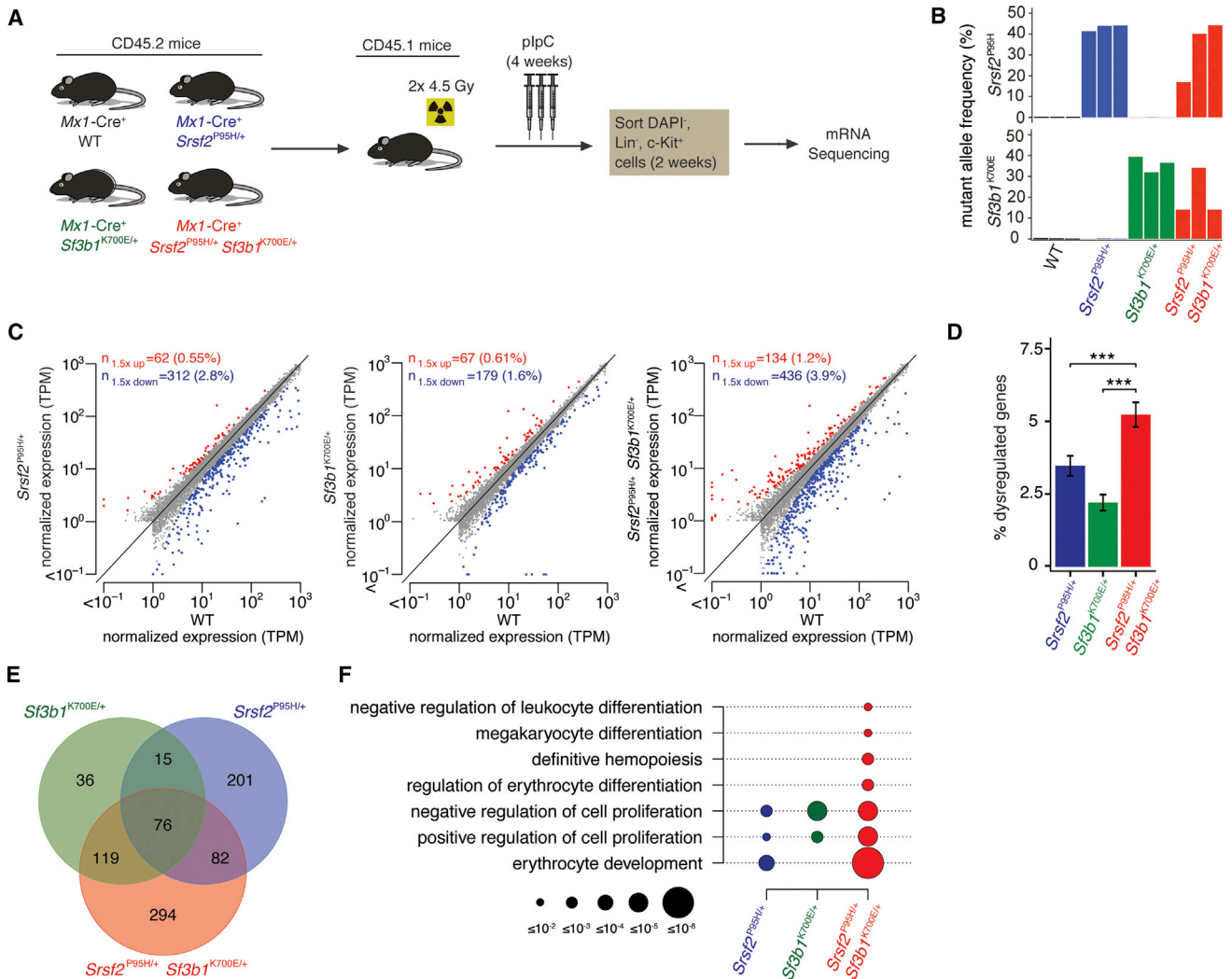


Figure 3. Srsf2 and Sf3b1 Mutations Have Distinct and Independent Effects on Gene Dysregulation

(A) Schema for RNA-seq.

(B) Expression of Srsf2^{P95H} and Sf3b1^{K700E} alleles as percentage of mRNAs expressed from Srsf2 and Sf3b1. Color indicates genotype; the three biological replicates are A to C from left to right.

(C) Scatterplots comparing coding gene expression in Mx1-Cre⁺ Srsf2^{P95H/+}, Mx1-Cre⁺ Sf3b1^{K700E/+}, and Mx1-Cre⁺ Srsf2^{P95H/+} Sf3b1^{K700E/+} cells relative to Mx1-Cre⁺ WT cells for replicate B. Red and blue indicate coding genes significantly up- or downregulated, respectively, in mutant relative to Mx1-Cre⁺ WT cells. TPM, transcripts per million (TMM-normalized).

(D) Bar plots comparing percentage of significantly dysregulated coding genes (percentage of total coding genes expressed) in Mx1-Cre⁺ Srsf2^{P95H/+}, Mx1-Cre⁺ Sf3b1^{K700E/+}, and Mx1-Cre⁺ Srsf2^{P95H/+} Sf3b1^{K700E/+} cells relative to Mx1-Cre⁺ WT cells for replicate B. Error bars represent mean ± SD. A two-sided binomial proportion test was used to compare groups; ***p < 0.0001.

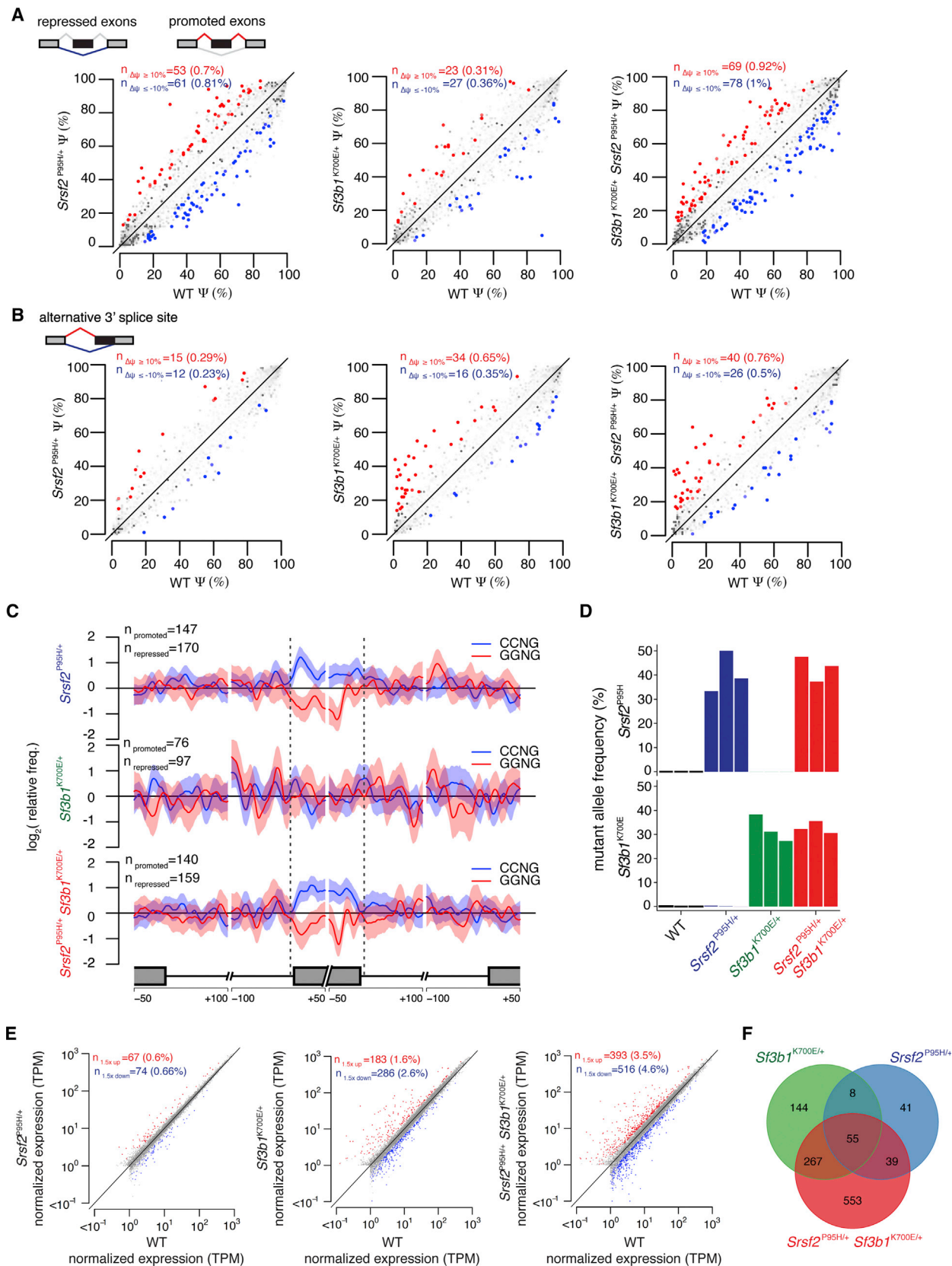
(E) Venn diagram showing overlap between coding genes significantly dysregulated in Mx1-Cre⁺ Srsf2^{P95H/+}, Mx1-Cre⁺ Sf3b1^{K700E/+}, and Mx1-Cre⁺ Srsf2^{P95H/+} Sf3b1^{K700E/+} cells relative to Mx1-Cre⁺ WT cells for replicate B.

(F) GO enrichment analysis of Mx1-Cre⁺ Srsf2^{P95H/+}, Mx1-Cre⁺ Sf3b1^{K700E/+}, and Mx1-Cre⁺ Srsf2^{P95H/+} Sf3b1^{K700E/+} cells relative to Mx1-Cre⁺ WT cells for replicate B. Circle size indicates the magnitude of the p value for each term and comparison.

See also Figure S3; Tables S2 and S3.

recapitulated the preferential effects of Sf3b1 and Srsf2 mutations on 3' splice site recognition and cassette exon recognition, respectively, that we observed in single-mutant cells (Figure S4A). We did not observe widespread decreases in splicing efficiency, such as retention of constitutive introns, in double-mutant cells (Figure S4E). Instead, Mx1-Cre⁺ Srsf2^{P95H/+} Sf3b1^{K700E/+} cells exhibited modest increases in mis-spliced

genes relative to cells bearing single mutations in Sf3b1 or Srsf2 (Figures 4A and 4B). Mx1-Cre⁺ Sf3b1^{K700E/+} Srsf2^{P95H/+} cells recapitulated 40% and 32% of splicing dysregulation driven by expression of the single mutations in Sf3b1^{K700E} and Srsf2^{P95H}, respectively (Figure S4F). We identified only seven genes mis-spliced in both Mx1-Cre⁺ Srsf2^{P95H/+} and Mx1-Cre⁺ Sf3b1^{K700E/+} single-mutant as well as double-mutant cells, and



(legend on next page)

only six genes mis-spliced in both *Mx1-Cre⁺ Srsf2^{P95H/+}* and *Mx1-Cre⁺ Sf3b1^{K700E/+}* single-mutant but not double-mutant cells. We therefore conclude that SF3B1 and SRSF2 mutations typically have distinct and independent consequences on splicing.

To confirm these findings, we performed RNA-seq on purified LK cells from E14.5 *Vav-Cre⁺ Srsf2^{P95H/+} Sf3b1^{K700E/+}* fetal liver and controls. The allelic frequencies of both mutations in double-mutant cells were near 50% and comparable with those of *Vav-Cre⁺* single-mutant controls (Figure 4D). Similar to the *Mx1-Cre* system, the greatest alterations in gene expression were seen in *Vav-Cre⁺ Srsf2^{P95H/+} Sf3b1^{K700E/+}* HSPCs compared with single-mutant controls, and double-mutant cells recapitulated much of the gene expression dysregulation in single-mutant cells (Figures 4E and 4F). GO analysis revealed signatures of impaired hematopoiesis in double-mutant cells, consistent with those seen in *Mx1-Cre* mice (Figure S4G and Table S5). Moreover, effects on splicing similar to those seen in the *Mx1-Cre* system were seen in HSPCs from *Vav-Cre* mice, including preferential effects of *Sf3b1* and *Srsf2* mutations on 3' splice site and cassette exon recognition, respectively (Figures S4H and S4I).

Combined Expression of *Srsf2* and *Sf3b1* Mutations Impairs Expression of Regulators of HSPC Survival and Increases Sensitivity to Inflammatory Stimulation

Given the largely non-overlapping effects of *Srsf2^{P95H}* and *Sf3b1^{K700E}* mutations on gene expression and splicing, we evaluated transcripts that exhibited concomitant dysregulation in gene expression and splicing in the double-mutant state (Figure 5A and Table S6). Multiple regulators of HSPC survival and quiescence were significantly dysregulated and mis-spliced in *Srsf2^{P95H/+} Sf3b1^{K700E/+}* HSPCs, including the thrombopoietin receptor *c-Mpl*, integrin α IIb (CD41), and the transcription factor *Pbx1* (Figures 5A and S5A). After confirming reduced expression of these transcripts in LK cells in an independent cohort of *Mx1-Cre⁺ Srsf2^{P95H/+} Sf3b1^{K700E/+}* mice (Figure 5B), we evaluated the consequences of short hairpin RNA (shRNA)-mediated depletion of these mRNAs in WT HSPCs (Figures S5B and S5C). Consistent with prior published data (Alexander et al., 1996; Ficara et al., 2008; Gekas and Graf, 2013; Qian et al., 2007; Yoshihara et al., 2007), silencing any of these individual genes was

associated with severe impairment of HSPC clonogenicity (Figure S5D).

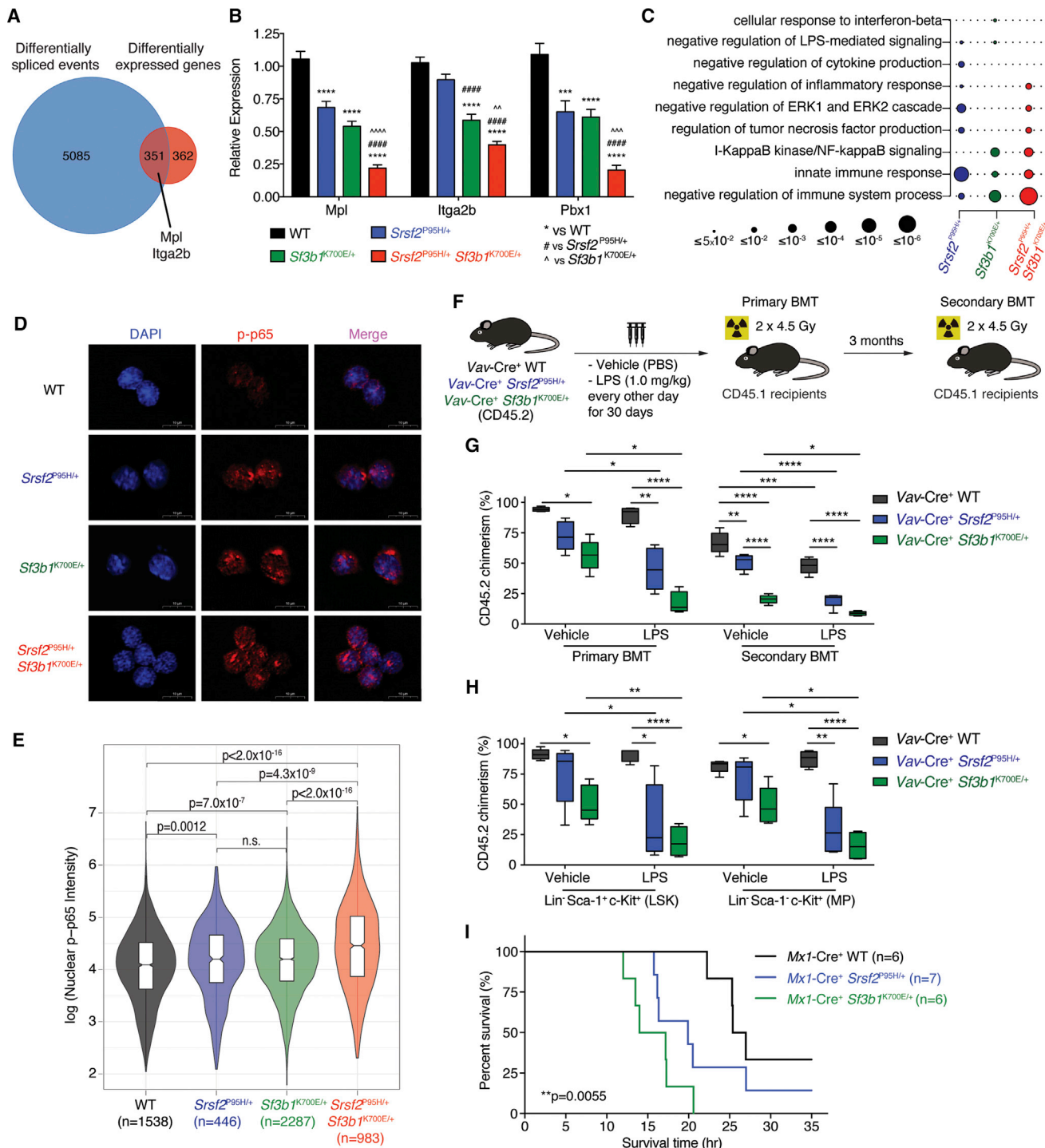
In addition to gene expression changes consistent with impaired hematopoiesis in *Srsf2^{P95H/+} Sf3b1^{K700E/+}* cells (Figure 3F), GO analysis also revealed a strong signature associated with immune signaling that was augmented in double- relative to single-mutant cells (Figures 5C and S4G). To functionally evaluate these gene expression changes, we studied the response of *Srsf2* and *Sf3b1* mutant cells to lipopolysaccharide (LPS). HSPCs from *Vav-Cre⁺ Srsf2^{P95H/+}* and *Vav-Cre⁺ Sf3b1^{K700E/+}* mice exhibited increased baseline nuclear factor κ B (NF- κ B) activation (marked by increased nuclear accumulation of phosphorylated p65 [p-p65]) relative to *Vav-Cre⁺* WT HSPCs (Figures 5D and 5E), and this was further enhanced following *ex vivo* LPS stimulation in double-mutant cells relative to single-mutant or WT cells (Figures S5E and S5F).

Given prior data identifying that chronic LPS exposure impairs repopulating potential of HSPCs (Esplin et al., 2011; Zhao et al., 2013), we next evaluated the effects of chronic inflammation on the function of *Srsf2* or *Sf3b1* mutant BM HSPCs (Figure 5F). *Vav-Cre⁺* WT, *Vav-Cre⁺ Srsf2^{P95H/+}*, and *Vav-Cre⁺ Sf3b1^{K700E/+}* mice were treated with LPS (1 mg/kg) every second day for 30 days followed by serial BMT into lethally irradiated recipient mice. Chronic LPS treatment had a mild effect on the repopulating potential of WT HSPCs, evidenced by similar peripheral blood and BM HSPC chimerism in primary recipients (Figures 5G and 5H). In contrast, LPS-treated *Vav-Cre⁺ Srsf2^{P95H/+}* and *Vav-Cre⁺ Sf3b1^{K700E/+}* BM HSPCs showed significant reduction in repopulating ability relative to vehicle-treated counterparts, and this defect was further exacerbated following serial transplantation (Figures 5G and 5H).

The above observations suggest that *Srsf2* and *Sf3b1* mutant HSPCs are intrinsically hypersensitive to inflammatory stimuli that contribute to defective hematopoietic function, rendering features observed in MDS patients. In addition, LPS-treated *Vav-Cre⁺ Srsf2^{P95H/+}* mice had enhanced myeloid skewing and reduced B lymphopoiesis relative to vehicle-treated mice or *Vav-Cre⁺ Srsf2^{+/+}* mice treated with LPS (Figure S5G). Moreover, acute *ex vivo* LPS stimulation of BM LSK cells from *Vav-Cre⁺ Srsf2^{P95H/+}* mice also resulted in significant increase in nuclear p-p65 relative to *Vav-Cre⁺ Srsf2^{+/+}* LSK cells (Figures S5H and S5I). The enhanced response to inflammatory stimuli in *Srsf2*

Figure 4. *Srsf2* and *Sf3b1* Mutations Have Distinct and Independent Effects on RNA Splicing

- (A) Scatterplots of cassette exon inclusion in *Mx1-Cre⁺ Srsf2^{P95H/+}*, *Mx1-Cre⁺ Sf3b1^{K700E/+}*, and *Mx1-Cre⁺ Srsf2^{P95H/+} Sf3b1^{K700E/+}* cells relative to *Mx1-Cre⁺* WT cells. Axes indicate the fraction of mRNAs containing each cassette exon in the indicated sample. Red and blue indicate cassette exons whose inclusion is promoted or repressed, respectively, in mutant relative to WT cells.
- (B) As in (A), but for alternative 3' splice site events. Axes indicate the fraction of mRNAs that use the intron-proximal 3' splice site in the indicated sample. Red and blue indicate intron-proximal 3' splice sites whose usage is promoted or repressed, respectively, in mutant relative to WT cells.
- (C) Plots illustrating the spatial distribution of the CCNG and GGNG (N = any nucleotide) exonic splicing enhancers adjacent to differentially spliced cassette exons promoted versus repressed in mutant relative to WT cells. Vertical axis indicates the relative frequency of each motif, averaged over all promoted versus repressed cassette exons for the indicated genotype comparisons.
- (D) Expression of *Srsf2^{P95H}* and *Sf3b1^{K700E}* alleles as percentage of mRNAs expressed from *Srsf2* and *Sf3b1* in lineage⁻ *c-Kit⁺* cells from fetal livers of *Vav-Cre* mice at E14.5. Color indicates genotype; the three biological replicates are A to C from left to right.
- (E) Scatterplots comparing mean coding gene expression for all replicates in *Vav-Cre⁺ Srsf2^{P95H/+}*, *Vav-Cre⁺ Sf3b1^{K700E/+}*, and *Vav-Cre⁺ Srsf2^{P95H/+} Sf3b1^{K700E/+}* cells relative to *Vav-Cre⁺* WT cells. Red and blue indicate coding genes significantly up- or downregulated, respectively, in mutant relative to *Vav-Cre⁺* WT cells. TPM, transcripts per million (TMM-normalized).
- (F) Venn diagram showing the overlap between coding genes significantly dysregulated in *Vav-Cre⁺ Srsf2^{P95H/+}*, *Vav-Cre⁺ Sf3b1^{K700E/+}*, and *Vav-Cre⁺ Srsf2^{P95H/+} Sf3b1^{K700E/+}* cells relative to *Vav-Cre⁺* WT cells in all replicates. See also Figure S4; Tables S4 and S5.



and *Sf3b1* mutant mice *in vivo* was evident upon LPS-induced sepsis. Exposure of primary *Mx1-Cre*⁺ WT, *Mx1-Cre*⁺ *Srsf2*^{P95H/+}, and *Mx1-Cre*⁺ *Sf3b1*^{K700E/+} mice with LPS (15 mg/kg) resulted in accelerated death in both *Srsf2*- and *Sf3b1*-mutant mice relative to WT controls (Figure 5I).

SF3B1 Mutations Promote Mis-splicing of MAP3K7, Resulting in Hyperactivation of NF-κB Signaling

The above results identify that spliceosomal mutations are intolerable when co-expressed but they are independently more sensitive to inflammatory stimuli that converge on NF-κB signaling. To understand how spliceosome gene mutations activate immune signaling pathways, we first focused on events that are mis-spliced within SF3B1-mutant hematopoietic cells in both human and mouse (Table S7). Although recent studies reported few such shared mis-spliced events (Mupo et al., 2016; Obeng et al., 2016), we identified a larger set of 205 transcripts mis-spliced in both *Sf3b1*-mutant murine hematopoietic cells and SF3B1-mutant MDS patients (Figure 6A). One of the most robust mis-spliced events was MAP3K7, for which an intron-proximal 3' splice site was promoted by mutant SF3B1 in both human and mouse hematopoietic cells. Reanalysis of RNA-seq data from CLL patient cohorts (DeBoever et al., 2015) and isogenic cell lines with endogenous mutations in SF3B1, as well as RT-PCR and Sanger sequencing of cDNA from SF3B1-mutant cells, validated this isoform (Figures 6B, 6C, and S6A). This aberrant 3' splice site recognition occurred in exon 5 of MAP3K7, which encodes part of the kinase domain, and is predicted to result in an out-of-frame transcript that undergoes nonsense-mediated decay (Figures S6B and S6C). Consistent with this, we observed reduced MAP3K7 protein in isogenic cell lines (Figures 6D and 6E) as well as patient BM mononuclear cells (MNCs) and peripheral blood MNCs from MDS and CLL patients, respectively (Figures 6F and 6G), with SF3B1 mutations versus those lacking splicing-factor mutations.

MAP3K7 encodes a kinase that mediates tumor necrosis factor α (TNFα), interleukin-1β (IL-1β), and Toll-like receptor signaling through the NF-κB, JNK, and MAPK pathways. The effects of MAP3K7 loss have been extensively studied and can result in loss or promotion of inflammation depending on cellular context (Ajibade et al., 2012; Lamothe et al., 2012; Sato et al., 2005; Tang et al., 2008; Vink et al., 2013; Xin et al., 2017). Here, we observed that SF3B1^{K700E} human myeloid or lymphoid leukemia cells stimulated with LPS had enhanced NF-κB activation compared with SF3B1 WT controls (Figures 6D, 6E, S6D, and S6E). Increased p-p65 level was also evident at baseline in isogenic cells as well as primary patient BM MNCs from SF3B1-mutant MDS and peripheral blood MNCs from SF3B1-mutant CLL relative to SF3B1 WT counterparts (Figures 6F and

6G). Increased nuclear p-p65 levels (Figure 7A) and enhanced NF-κB transcriptional activity using a reporter assay (Figures 7B and S7A) were also evident in SF3B1^{K700E} cells compared with SF3B1 WT cells following LPS or TNFα stimulation. This was further confirmed by marked induction in NF-κB targets IL-1β and TNFα following LPS treatment in SF3B1^{K700E} NALM-6 cells relative to parental and SF3B1^{K700K} control cells (Figure 7C).

Given that a number of aberrant splicing and gene expression events occur in SF3B1-mutant cells, we next sought to understand the contribution of MAP3K7 loss to hyperactivated NF-κB signaling. First, hyperactive NF-κB signaling was confirmed using shRNA-mediated downregulation of MAP3K7 in NALM-6 and K562 parental cells at the level of p-p65 signaling and NF-κB transcriptional activity at both baseline and after LPS stimulation (Figures 7B and S7B). In addition, re-expression of MAP3K7 in K562 SF3B1^{K700E} cells resulted in a significant decrease in p-p65 in both resting state as well as following LPS exposure based on immunoblotting, NF-κB luciferase reporter, and nuclear p-p65 level (Figures 7D, 7F, and S7C). At a biological level, restoration of Map3k7 expression in *Sf3b1*^{K700E/+} HSPCs resulted in mild rescue of HSPC clonogenicity (Figure S7D). Overall, these data suggest that the effects of SF3B1^{K700E} mutation on induction of NF-κB signaling are indeed, in part, mediated through aberrant splicing of MAP3K7.

SRSF2 Mutations Promote Aberrant Splicing of Caspase-8, Resulting in a Truncated Protein that Hyperactivates NF-κB Signaling

Consistent with the distinct effects of SF3B1 and SRSF2 mutations on splicing, MAP3K7 aberrant splicing was restricted to SF3B1-mutant cells (Figure S8A). We therefore searched for aberrant splicing events in SRSF2-mutant cells that might affect NF-κB signaling. One such event was aberrant splicing of caspase-8, encoded by CASP8, that was recurrently mis-spliced in AML and CMML patients with SRSF2 mutations, but not those bearing SF3B1 mutations (Figures 8A and S8B). Caspase-8 is a cysteine protease that initiates death-receptor-mediated apoptosis (Shu et al., 1997; Thome et al., 1997) in addition to regulating necroptosis and serving as a key activator of NF-κB (Chaudhary et al., 2000; Hu et al., 2000; Shikama et al., 2003). SRSF2 mutations repressed a cassette exon of caspase-8, as was evident by RNA-seq, RT-PCR, qRT-PCR, and cDNA sequencing from cell lines and patient samples (Figures 8A, 8B, and S8C–S8E). CASP8 normally encodes a 54/55-kDa protein containing two death-effector domains (DED) at the N terminus and a C-terminal catalytic domain. Exclusion of this cassette exon results in an mRNA encoding a truncated caspase-8 protein lacking the C-terminal catalytic domains, which was readily

(E) Violin plots quantifying nuclear p-p65 intensity of LK cells from (D). ANOVA and Kruskal-Wallis ranked test was performed and adjusted for false discovery rate.

(F) Schema of competitive BMT using BM MNCs from *Vav-Cre*⁺ WT, *Vav-Cre*⁺ *Srsf2*^{P95H/+}, and *Vav-Cre*⁺ *Sf3b1*^{K700E/+} mice after chronic LPS exposure.

(G) Percentage of CD45.2 chimerism in peripheral blood of recipients (n = 4–5 mice per group) from primary and secondary BMT (both at 10 weeks post BMT).

(H) Chimerism of LSK or myeloid progenitor (MP; lineage[−] Sca-1[−] c-Kit⁺) fractions from primary recipients 14 weeks post BMT.

(I) Kaplan-Meier analysis of *Mx1-Cre*⁺ WT, *Mx1-Cre*⁺ *Srsf2*^{P95H/+}, and *Mx1-Cre*⁺ *Sf3b1*^{K700E/+} mice after a single dose of LPS (15 mg/kg) *in vivo*. Log-rank Mantel-Cox test was performed. **p = 0.0055.

ANOVA and Tukey's post hoc test were used to compare groups. *p < 0.05, **p < 0.01, ***p < 0.001, ****p < 0.0001 versus *Vav-Cre*⁺ WT mice (“#” denotes versus *Vav-Cre*⁺ *Srsf2*^{P95H/+} mice and “^” denotes versus *Vav-Cre*⁺ *Sf3b1*^{K700E/+} mice). In (G) and (H), the top and bottom lines of the box represent the upper and lower quartiles, respectively; the line inside the box represents the median; the lines above and below the box represent the maximum and minimum values, respectively. See also Figure S5 and Table S6.

detectable in *SRSF2*-mutant cells using an N-terminal anti-caspase-8 antibody (Figures 8C and 8D). Although several caspase-8 isoforms have been described (Xu et al., 2009; Yuan et al., 2012), the specific isoform detected in *SRSF2*-mutant cells is distinct from those previously described.

Previously described DED-only forms of caspase-8 have been suggested to serve either as competitive inhibitors or promoters of apoptosis (Xu et al., 2009; Yuan et al., 2012). Given this, we tested the effect of this *SRSF2*-mutant-specific truncated isoform (hereafter referred to as CASP8^{TR}) in an *SRSF2* WT cell line followed by TRAIL (TNF-related apoptosis-inducing ligand) stimulation to engage the death-receptor pathway. Overexpression of both caspase-8 full-length (CASP8^{FL}) and CASP8^{TR} isoforms resulted in robust expression of proteins at the expected size (Figures 8E and S8F) with no effect on cell growth (Figure S8G). Moreover, both isoforms promoted TRAIL-mediated cell death, suggesting that the truncated isoform did not affect cell death relative to CASP8^{FL} (Figure S8H). Given this, we next evaluated the effect of overexpressing CASP8^{TR} on NF- κ B transcriptional activity, signaling, and nuclear localization. In both K562 and HAP1 cells with endogenous caspase-8 expression, overexpression of the CASP8^{TR}, but not the CASP8^{FL} isoform, resulted in robust induction of NF- κ B activity upon increasing concentration of TRAIL (Figures 8E, 8F, S8I, and S8J). These data were also confirmed in K562 cells with or without endogenous *SRSF2*^{P95H} mutation (Figures 8G, S8K, and S8L). To rule out an effect of endogenous caspase-8, we assessed the effect of CASP8^{TR} on cell death and NF- κ B activity in CASP8^{KO} HAP1 cells. Consistent with the lack of the catalytic domain, CASP8^{KO} HAP1 cells expressing CASP8^{TR} isoform were unable to undergo TRAIL-mediated cell death (Figures S8M and S8N); however, the CASP8^{TR} isoform was able to induce robust NF- κ B signaling in the absence of WT caspase-8 (Figures 8F, S8O, and S8P).

DISCUSSION

Mutations affecting RNA splicing factors are the most common genetic alterations in MDS but the basis for their significant enrichment in this disease remains largely unexplained. Here we identify that two of the most commonly mutated splicing factors in MDS converge on activation of innate immune signaling through aberrant splicing of mRNAs encoding distinct enzymes.

Although the initial description of spliceosomal mutations predicted that the mutually exclusive pattern of these mutations might be due to a common impact on MDS pathogenesis (Yoshida et al., 2011), the data here identify that these mutations are mutually exclusive, in part due to synthetic lethal interaction. This provides one of the few examples of mutually exclusive oncogenic alterations due to synthetic lethal interactions in cancer. Interestingly, co-expression of SF3B1^{K700E} and *SRSF2*^{P95H} mutations resulted in impaired HSPC self-renewal, differentiation, and survival, but this is not due to widespread inhibition of

splicing efficiency. Instead we identified aberrant splicing and dysregulation of key regulators of HSPC function in double-mutant cells, including the thrombopoietin receptor c-Mpl, the homeodomain transcription factor Pbx1, and integrin α Lb. Hematopoietic-specific deletion of these factors individually has previously been shown to result in failure of hematopoiesis due to reduced HSC self-renewal, increased apoptosis, and loss of quiescence (Ficara et al., 2008; Gekas and Graf, 2013; Qian et al., 2007; Yoshihara et al., 2007), all features characteristic of the double-mutant state.

Multiple lines of evidence implicate innate immune signaling in MDS pathogenesis (Basiorka et al., 2016; Fang et al., 2014; Wei et al., 2013), including experiments demonstrating increased innate immune signaling contributes to MDS development *in vivo* (Fang et al., 2017; Varney et al., 2015). Increased activation of Toll-like receptor and IL-1 receptor signaling with downstream activation of MAPK and NF- κ B pathways is widely reported in MDS, but the mechanistic basis for this activation have mostly been restricted to MDS with deletion of chromosome 5q (Fang et al., 2014, 2017; Starczynowski, 2014; Varney et al., 2015). Our work identifies a mechanism for hyperactivated NF- κ B signaling in a wider spectrum of MDS.

Although recent studies of SF3B1^{K700E} mutation identified relatively few mRNAs mis-spliced in both mouse and human cells (Mupo et al., 2016; Obeng et al., 2016), we identified a much greater overlap of aberrantly spliced transcripts shared across mouse and human SF3B1^{K700E} mutant hematopoietic cells than previously reported. This includes aberrant splicing of MAP3K7 through the use of an alternative 3' splice site promoted by mutant SF3B1. As downregulation of Map3k7 in myeloid cells promotes myeloid neoplasms, this finding is likely to be relevant to SF3B1-mutant MDS. For example, *in vivo* knockdown of Map3k7 resulted in splenomegaly, myeloproliferation, and extramedullary hematopoiesis, as well as increased immune activation that was exacerbated by LPS (Vink et al., 2013). Similarly, myeloid-specific deletion of *Map3k7* heightened the response to inflammatory stimuli and causes a clonal myeloid leukemia (Ajibade et al., 2012; Eftychi et al., 2012; Lamothe et al., 2012; Xin et al., 2017). Interestingly, the pro-inflammatory and leukemogenic effects of *Map3k7* loss appear to be restricted to myeloid lineages (Ajibade et al., 2012), in stark contrast to pan-hematopoietic deletion of *Map3k7*, which results in complete failure of hematopoiesis (Tang et al., 2008). It will therefore be important to understand whether there is a differential requirement for hematopoiesis in SF3B1 mutant cells given the partial loss of MAP3K7 induced by mutant SF3B1.

While aberrant splicing and downregulation of MAP3K7 was specific to SF3B1 mutant cells, cells expressing mutant *SRSF2* shared similar elevated innate immune signaling and hypersensitivity to LPS. This led us to identify a gain-of-function effect of *SRSF2* mutations through generation of a C-terminal truncated caspase-8 isoform that promotes NF- κ B signaling. This is

(C) RT-PCR of the MAP3K7 competing 3' splice site in MDS and CLL patient samples with or without SF3B1 mutations as well as isogenic human and mouse cells. (D and E) Immunoblot of phosphorylated p65 (p-p65), I κ B- α , MAP3K7, and loading controls in isogenic K562 (D) and NALM-6 (E) cells. "Time (hr)" refers to hours following LPS (5 μ g/mL) exposure.

(F and G) Immunoblot analysis of p-p65, MAP3K7, and loading controls in BM MNCs from MDS (F) and peripheral blood MNCs from CLL patients (G) with or without SF3B1 mutations.

See also Figure S6 and Table S7.

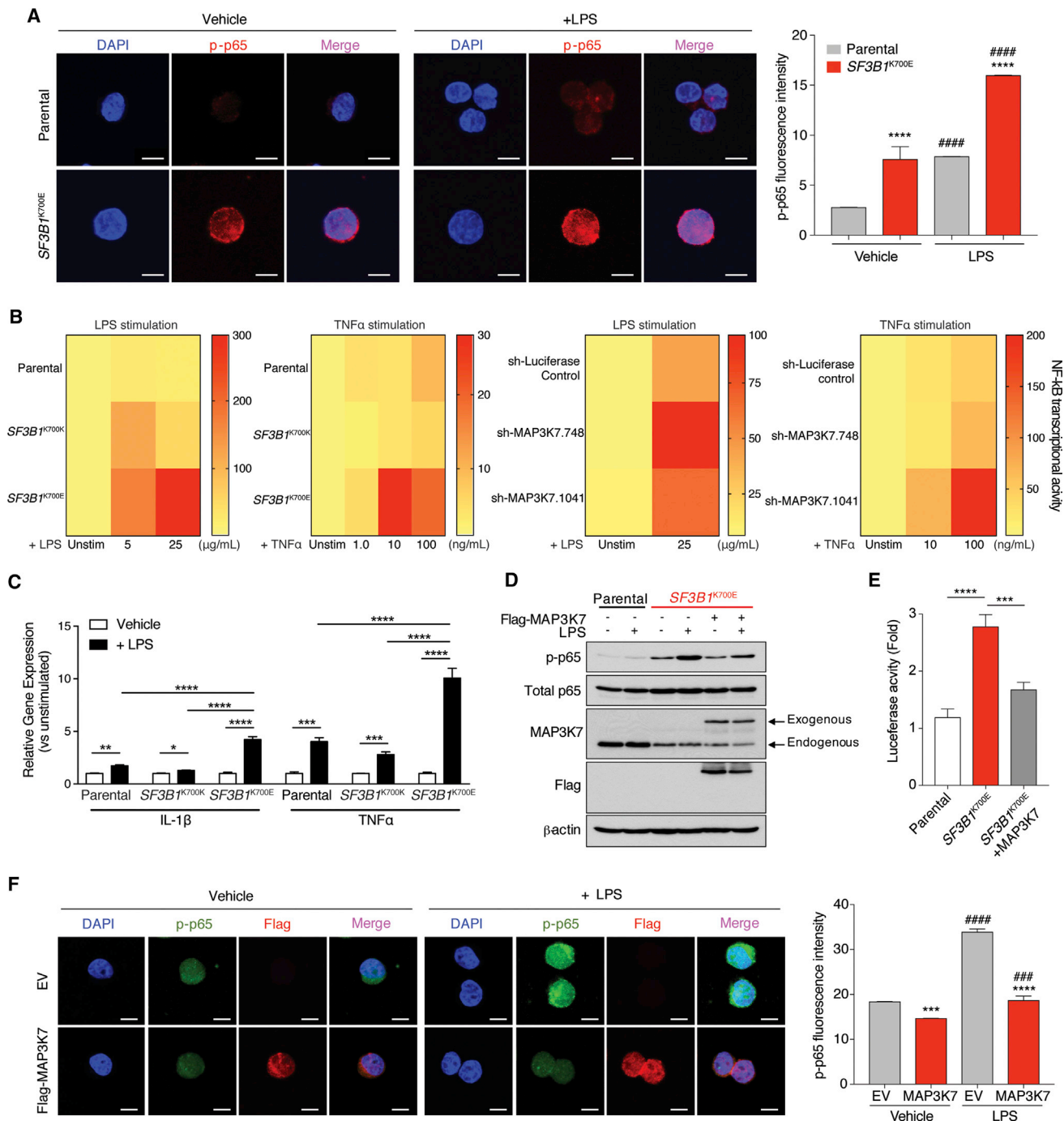


Figure 7. MAP3K7 Loss Results in Hyperactive NF- κ B Signaling in *SF3B1*-Mutant Cells

(A) Immunofluorescence of phosphorylated p65 (p-p65) in K562 cells with or without *SF3B1*^{K700E} mutation 2 hr following LPS stimulation. Quantitation of p-p65 intensity is shown on the right (n = 3 independent experiments). Scale bars, 10 μ m.

(B) Heatmap of NF- κ B reporter signal in NALM-6 *SF3B1*-isogenic cells (left two panels) or parental NALM-6 cells with MAP3K7 shRNAs (right two panels) following LPS or TNF α stimulation for 24 hr.

(C) qRT-PCR analysis of IL-1 β and TNF α 8 hr post LPS stimulation in NALM-6 *SF3B1*-isogenic cells (n = 2 independent experiments).

(D) Immunoblot of p-p65 in K562 *SF3B1*-isogenic cells \pm FLAG-MAP3K7 cDNA and/or LPS (5 μ g/mL) exposure for 2 hr.

(E) Quantitation of NF- κ B reporter signal in cells from (D) (n = 3 independent experiments).

(F) Immunofluorescence of nuclear p-p65 and FLAG (MAP3K7) in cells from (D) (quantitation of p-p65 intensity [n = 3 independent experiments] on the right). Scale bars, 10 μ m.

Error bars represent mean \pm SD. ANOVA followed by Tukey's post hoc test were used to compare groups. *p < 0.05, **p < 0.005, ***p < 0.0002, ****p < 0.0001, #####p < 0.0001 versus Vehicle; ###p < 0.001 versus Vehicle. See also Figure S7.

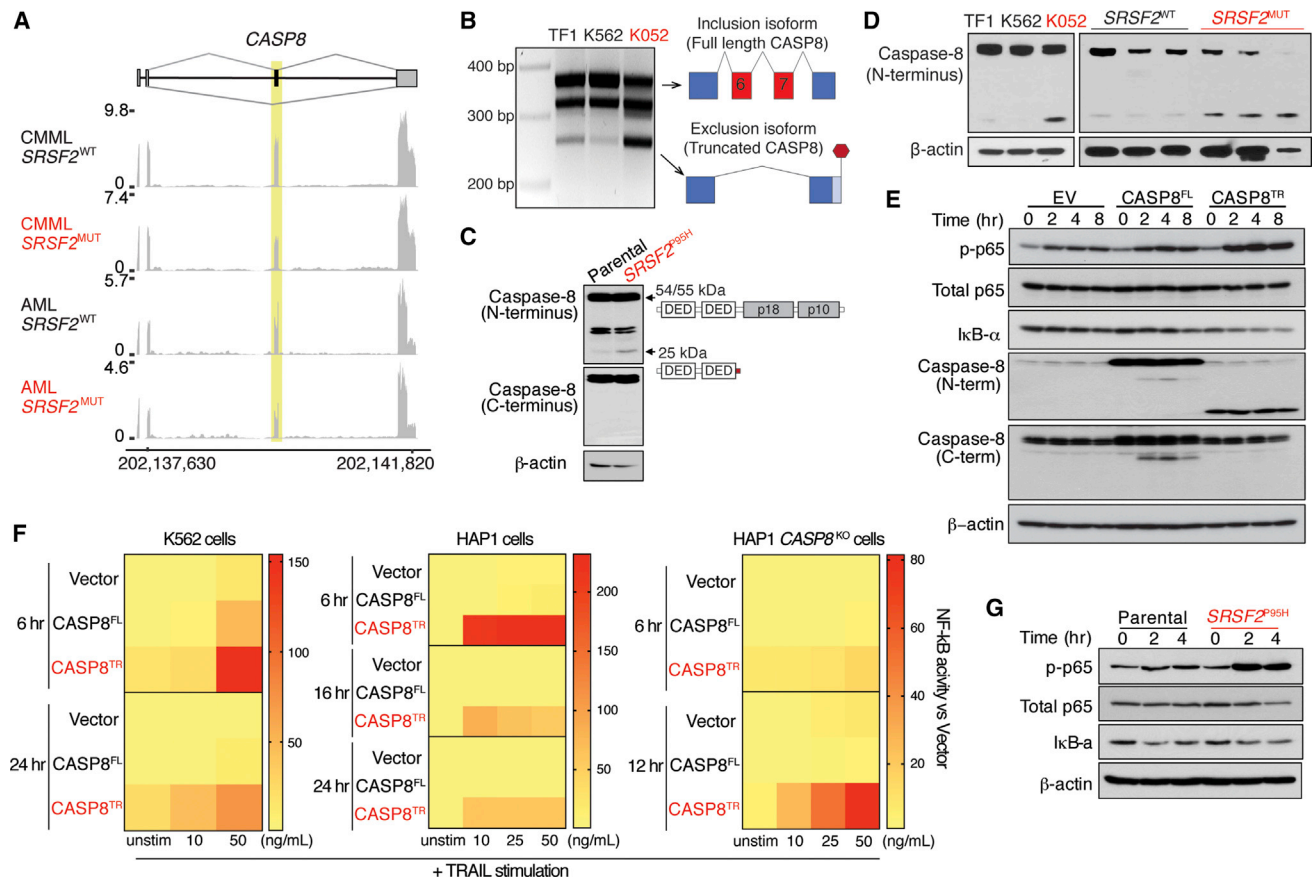


Figure 8. *SRSF2* Mutations Promote Aberrant Splicing of Caspase-8, Resulting in Expression of a Truncated Protein that Hyperactivates NF- κ B Signaling

(A) RNA-seq coverage plots of caspase-8 splicing in CMMML and AML patients WT or mutant (MUT) for *SRSF2*.

(B) RT-PCR analysis of caspase-8 splicing in *SRSF2* WT (TF1 and K562) or *SRSF2*-mutant (K052) cells.

(C and D) Immunoblot of caspase-8 using an N-terminal anti-caspase-8 antibody in K562 *SRSF2*-isogenic cells (C) or primary AML patient samples (right panel) WT or mutant for *SRSF2* (D).

(E) Immunoblot of phosphorylated p65 (p-p65), I κ B- α , caspase-8 in K562 cells expressing empty vector (EV), full-length caspase-8 (*CASP8*^{FL}), or the truncated caspase-8 isoform (*CASP8*^{TR}) after exposure to TRAIL (50 ng/mL).

(F) Heatmap of NF- κ B reporter signal following TRAIL stimulation in K562, HAP1, or *CASP8*^{KO} HAP1 cells expressing EV, *CASP8*^{FL}, or *CASP8*^{TR}.

(G) Immunoblot of p-p65 and I κ B- α in K562 cells with or without *SRSF2*^{P95H} following exposure to TRAIL (50 ng/mL).

See also Figure S8.

consistent with prior work showing that N-terminal prodomain-only containing isoforms of procaspase-8 activate NF- κ B signaling through interactions with upstream regulators of NF- κ B, a function not mediated by canonical full-length caspase-8 (Chaudhary et al., 2000; Hu et al., 2000; Shikama et al., 2003).

Together, our data demonstrate that different splicing-factor mutations alter distinct targets at the level of pre-mRNA splicing that nonetheless converge on the same downstream signaling node to hyperactivate innate immune signaling.

STAR★METHODS

Detailed methods are provided in the online version of this paper and include the following:

- KEY RESOURCES TABLE
- CONTACT FOR REAGENT AND RESOURCE SHARING

● EXPERIMENTAL MODEL AND SUBJECT DETAILS

- Animals
- Primary Human MDS and CLL Samples
- Cell Lines

● METHOD DETAILS

- Peripheral Blood Analysis
- Bone Marrow Transplantation Assays
- *In Vivo* LPS Stimulation Experiment
- *In Vitro* Colony-Forming Assays
- Flow Cytometry Analyses
- Cell Cycle and Apoptosis Analyses
- Histological Analysis
- Immunoblot
- Immunofluorescence
- Caspase-8 and MAP3K7 Constructs
- mRNA Stability Assay
- Luciferase Reporter Assay

- RT-PCR and Quantitative RT-PCR (qRT-PCR)
- shRNA Experiments
- mRNA Isolation, Sequencing, and Analysis
- Genome Annotations
- RNA-seq Read Mapping
- Differential Gene Expression Analysis
- Differential Splicing Analysis
- Gene Ontology (GO) Enrichment Analysis
- Motif Enrichment Analysis and Sequence Logos
- Analysis of Expected and Observed Gene Expression Convergence
- **QUANTIFICATION AND STATISTICAL ANALYSIS**
 - Statistical Analyses
- **DATA AND SOFTWARE AVAILABILITY**
 - Publicly Available RNA-seq Data
 - Accession Codes

SUPPLEMENTAL INFORMATION

Supplemental Information includes eight figures and eight tables and can be found with this article online at <https://doi.org/10.1016/j.ccell.2018.07.003>.

ACKNOWLEDGMENTS

This work was supported by the Leukemia and Lymphoma Society (S.C.-W.L., D.I., R.K.B., O.A.-W.), the NCI K99 CA218896 (S.C.-W.L.), Aplastic Anemia and MDS International Foundation (A.Y.), Lauri Strauss Leukemia Foundation (A.Y.), US Dept. of Defense Bone Marrow Failure Research Program grant W81XWH-12-1-0041 (R.K.B., O.A.-W.), the National Research Foundation of Korea (NRF) grant funded by the Korean Government (Young Researcher Program, NRF-2017R1C1B2001991) (E.K.), the Settlement Research Fund (1.160104.01) of UNIST (Ulsan National Institute of Science and Technology) (E.K.), the NRF grant (the Individual Research in Basic Science and Engineering program, NRF-2017R1D1A1B03034094) (E.J.), the American Society of Hematology (S.C.-W.L., J.T., B.H.D., O.A.-W.), the Edward P. Evans Foundation (R.K.B., O.A.-W.), the Taub Foundation (O.A.-W.), grant R01 HL128239 (R.K.B., O.A.-W.), the Ellison Medical Foundation grant AG-NS-1030-13 (R.K.B.), grant R01 DK103854 (R.K.B.), the Starr Foundation grants I8-A8-075 and I9-A9-059 (O.A.-W.), and The Pershing Square Sohn Foundation. We would like to acknowledge the Molecular Cytology, Flow Cytometry, and Laboratory of Comparative Pathology core facilities for their technical assistance, and the MSK Cancer Center Support grant P30 CA008748.

AUTHOR CONTRIBUTIONS

S.C.-W.L., K.N., E.K., R.K.B., and O.A.-W. designed the study. S.C.-W.L., K.N., E.K., E.J., S.X.L., B.L., D.I., A.Y., M.K., M.Y., X.J.Z., M.K.K., H.C., Y.R.C., J.T., B.H.D., S.M., and Y.J.K. performed experiments. S.C.-W.L., K.N., E.K., E.J., S.X.L., B.L., D.I., A.P., J.P., M.S., S.B., P.G.S., and R.K.B. analyzed data. E.O. and B.L.E. provided the *Sf3b1*^{K700E} mouse. S.C.-W.L., K.N., R.K.B., and O.A.-W. prepared the manuscript with help from all co-authors.

DECLARATION OF INTERESTS

J.P., M.S., S.B., and P.G.S. are employees of H3 Biomedicine.

Received: May 11, 2017

Revised: April 25, 2018

Accepted: July 12, 2018

Published: August 13, 2018

REFERENCES

Ajibade, A.A., Wang, Q., Cui, J., Zou, J., Xia, X., Wang, M., Tong, Y., Hui, W., Liu, D., Su, B., et al. (2012). TAK1 negatively regulates NF-kappaB and p38 MAP kinase activation in Gr-1^{CD11b} neutrophils. *Immunity* 36, 43–54.

Alexander, W.S., Roberts, A.W., Nicola, N.A., Li, R., and Metcalf, D. (1996). Deficiencies in progenitor cells of multiple hematopoietic lineages and defective megakaryocytopoiesis in mice lacking the thrombopoietic receptor c-Mpl. *Blood* 87, 2162–2170.

Basiorka, A.A., McGraw, K.L., Eksioğlu, E.A., Chen, X., Johnson, J., Zhang, L., Zhang, Q., Irvine, B.A., Cluzeau, T., Sallman, D.A., et al. (2016). The NLRP3 inflammasome functions as a driver of the myelodysplastic syndrome phenotype. *Blood* 128, 2960–2975.

Bejar, R., Stevenson, K.E., Caughey, B.A., Abdel-Wahab, O., Steensma, D.P., Galili, N., Raza, A., Kantarjian, H., Levine, R.L., Neuberg, D., et al. (2012). Validation of a prognostic model and the impact of mutations in patients with lower-risk myelodysplastic syndromes. *J. Clin. Oncol.* 30, 3376–3382.

Chaudhary, P.M., Eby, M.T., Jasmin, A., Kumar, A., Liu, L., and Hood, L. (2000). Activation of the NF-kappaB pathway by caspase 8 and its homologs. *Oncogene* 19, 4451–4460.

Damm, F., Kosmider, O., Gelsi-Boyer, V., Renneville, A., Carbuccia, N., Hidalgo-Curtis, C., Della Valle, V., Couronné, L., Scourciz, L., Chesnais, V., et al. (2012). Mutations affecting mRNA splicing define distinct clinical phenotypes and correlate with patient outcome in myelodysplastic syndromes. *Blood* 119, 3211–3218.

Darman, R.B., Seiler, M., Agrawal, A.A., Lim, K.H., Peng, S., Aird, D., Bailey, S.L., Bhavsar, E.B., Chan, B., Colla, S., et al. (2015). Cancer-associated SF3B1 hotspot mutations induce cryptic 3' splice site selection through use of a different branch point. *Cell Rep.* 13, 1033–1045.

DeBoever, C., Ghia, E.M., Shepard, P.J., Rassenti, L., Barrett, C.L., Jepsen, K., Jamieson, C.H., Carson, D., Kipps, T.J., and Frazer, K.A. (2015). Transcriptome sequencing reveals potential mechanism of cryptic 3' splice site selection in SF3B1-mutated cancers. *PLoS Comput. Biol.* 11, e1004105.

Dolatshad, H., Pellagatti, A., Fernandez-Mercado, M., Yip, B.H., Malcovati, L., Attwood, M., Przychodzen, B., Sahgal, N., Kanapin, A.A., Lockstone, H., et al. (2015). Disruption of SF3B1 results in deregulated expression and splicing of key genes and pathways in myelodysplastic syndrome hematopoietic stem and progenitor cells. *Leukemia* 29, 1092–1103.

Dvinge, H., Ries, R.E., Ilagan, J.O., Stirewalt, D.L., Meshinchi, S., and Bradley, R.K. (2014). Sample processing obscures cancer-specific alterations in leukemic transcriptomes. *Proc. Natl. Acad. Sci. USA* 111, 16802–16807.

Eftychi, C., Karagianni, N., Alexiou, M., Apostolaki, M., and Kollias, G. (2012). Myeloid TAK1 [corrected] acts as a negative regulator of the LPS response and mediates resistance to endotoxemia. *PLoS One* 7, e31550.

Esplin, B.L., Shimazu, T., Welner, R.S., Garrett, K.P., Nie, L., Zhang, Q., Humphrey, M.B., Yang, Q., Borghesi, L.A., and Kincaid, P.W. (2011). Chronic exposure to a TLR ligand injures hematopoietic stem cells. *J. Immunol.* 186, 5367–5375.

Fang, J., Barker, B., Bolanos, L., Liu, X., Jerez, A., Makishima, H., Christie, S., Chen, X., Rao, D.S., Grimes, H.L., et al. (2014). Myeloid malignancies with chromosome 5q deletions acquire a dependency on an intrachromosomal NF-kappaB gene network. *Cell Rep.* 8, 1328–1338.

Fang, J., Bolanos, L.C., Choi, K., Liu, X., Christie, S., Akunuru, S., Kumar, R., Wang, D., Chen, X., Greis, K.D., et al. (2017). Ubiquitination of hnRNPA1 by TRAF6 links chronic innate immune signaling with myelodysplasia. *Nat. Immunol.* 18, 236–245.

Fellmann, C., Hoffmann, T., Sridhar, V., Hopfgartner, B., Muhar, M., Roth, M., Lai, D.Y., Barbosa, I.A., Kwon, J.S., Guan, Y., et al. (2013). An optimized microRNA backbone for effective single-copy RNAi. *Cell Rep.* 5, 1704–1713.

Ficara, F., Murphy, M.J., Lin, M., and Cleary, M.L. (2008). Pbx1 regulates self-renewal of long-term hematopoietic stem cells by maintaining their quiescence. *Cell Stem Cell* 2, 484–496.

Flicek, P., Ahmed, I., Amode, M.R., Barrell, D., Beal, K., Brent, S., Carvalho-Silva, D., Clapham, P., Coates, G., Fairley, S., et al. (2013). Ensembl 2013. *Nucleic Acids Res.* 41, D48–D55.

Gekas, C., and Graf, T. (2013). CD41 expression marks myeloid-biased adult hematopoietic stem cells and increases with age. *Blood* 121, 4463–4472.

Haferlach, T., Nagata, Y., Grossmann, V., Okuno, Y., Bacher, U., Nagae, G., Schnittger, S., Sanada, M., Kon, A., Alpermann, T., et al. (2014). Landscape

- of genetic lesions in 944 patients with myelodysplastic syndromes. *Leukemia* 28, 241–247.
- Harbour, J.W., Roberson, E.D., Anbunathan, H., Onken, M.D., Worley, L.A., and Bowcock, A.M. (2013). Recurrent mutations at codon 625 of the splicing factor SF3B1 in uveal melanoma. *Nat. Genet.* 45, 133–135.
- Hu, W.H., Johnson, H., and Shu, H.B. (2000). Activation of NF-kappaB by FADD, casper, and caspase-8. *J. Biol. Chem.* 275, 10838–10844.
- Huber, W., Carey, V.J., Gentleman, R., Anders, S., Carlson, M., Carvalho, B.S., Bravo, H.C., Davis, S., Gatto, L., Girke, T., et al. (2015). Orchestrating high-throughput genomic analysis with bioconductor. *Nat. Methods* 12, 115–121.
- Hubert, C.G., Bradley, R.K., Ding, Y., Toledo, C.M., Herman, J., Skutt-Kakaria, K., Girard, E.J., Davison, J., Berndt, J., Corrin, P., et al. (2013). Genome-wide RNAi screens in human brain tumor isolates reveal a novel viability requirement for PHF5A. *Genes Dev.* 27, 1032–1045.
- Ilagan, J.O., Ramakrishnan, A., Hayes, B., Murphy, M.E., Zebari, A.S., Bradley, P., and Bradley, R.K. (2014). U2AF1 mutations alter splice site recognition in hematological malignancies. *Genome Res.* 25, 14–26.
- Katz, Y., Wang, E.T., Airoidi, E.M., and Burge, C.B. (2010). Analysis and design of RNA sequencing experiments for identifying isoform regulation. *Nat. Methods* 7, 1009–1015.
- Kim, E., Ilagan, J.O., Liang, Y., Daubner, G.M., Lee, S.C., Ramakrishnan, A., Li, Y., Chung, Y.R., Micol, J.B., Murphy, M.E., et al. (2015). SRSF2 mutations contribute to myelodysplasia by mutant-specific effects on exon recognition. *Cancer Cell* 27, 617–630.
- Lamothe, B., Lai, Y., Hur, L., Orozco, N.M., Wang, J., Campos, A.D., Xie, M., Schneider, M.D., Lockworth, C.R., Jakacky, J., et al. (2012). Deletion of TAK1 in the myeloid lineage results in the spontaneous development of myelomonocytic leukemia in mice. *PLoS One* 7, e51228.
- Langmead, B., Trapnell, C., Pop, M., and Salzberg, S.L. (2009). Ultrafast and memory-efficient alignment of short DNA sequences to the human genome. *Genome Biol.* 10, R25.
- Lasho, T.L., Jimma, T., Finke, C.M., Patnaik, M., Hanson, C.A., Ketterling, R.P., Pardanani, A., and Tefferi, A. (2012). SRSF2 mutations in primary myelofibrosis: significant clustering with IDH mutations and independent association with inferior overall and leukemia-free survival. *Blood* 120, 4168–4171.
- Lee, S.C., Dvinge, H., Kim, E., Cho, H., Micol, J.B., Chung, Y.R., Durham, B.H., Yoshimi, A., Kim, Y.J., Thomas, M., et al. (2016). Modulation of splicing catalysis for therapeutic targeting of leukemia with mutations in genes encoding spliceosomal proteins. *Nat. Med.* 22, 672–678.
- Li, B., and Dewey, C.N. (2011). RSEM: accurate transcript quantification from RNA-Seq data with or without a reference genome. *BMC Bioinformatics* 12, 323.
- Makishima, H., Visconte, V., Sakaguchi, H., Jankowska, A.M., Abu Kar, S., Jerez, A., Przychodzen, B., Bupathi, M., Guinta, K., Afable, M.G., et al. (2012). Mutations in the spliceosome machinery, a novel and ubiquitous pathway in leukemogenesis. *Blood* 119, 3203–3210.
- Martin, M., Masshofer, L., Temming, P., Rahmann, S., Metz, C., Bornfeld, N., van de Nes, J., Klein-Hitpass, L., Hinnebusch, A.G., Horsthemke, B., et al. (2013). Exome sequencing identifies recurrent somatic mutations in EIF1AX and SF3B1 in uveal melanoma with disomy 3. *Nat. Genet.* 45, 933–936.
- Meggendorfer, M., Roller, A., Haferlach, T., Eder, C., Dicker, F., Grossmann, V., Kohlmann, A., Alpermann, T., Yoshida, K., Ogawa, S., et al. (2012). SRSF2 mutations in 275 cases with chronic myelomonocytic leukemia (CMML). *Blood* 120, 3080–3088.
- Meyer, L.R., Zweig, A.S., Hinrichs, A.S., Karolchik, D., Kuhn, R.M., Wong, M., Sloan, C.A., Rosenbloom, K.R., Roe, G., Rhead, B., et al. (2013). The UCSC Genome Browser database: extensions and updates 2013. *Nucleic Acids Res.* 41, D64–D69.
- Mupo, A., Seiler, M., Sathiaseelan, V., Pance, A., Yang, Y., Agrawal, A.A., Iorio, F., Bautista, R., Pacharne, S., Tzelepis, K., et al. (2016). Hemopoietic-specific Sf3b1-K700E knock-in mice display the splicing defect seen in human MDS but develop anemia without ring sideroblasts. *Leukemia* 31, 720–727.
- Obeng, E.A., Chappell, R.J., Seiler, M., Chen, M.C., Campagna, D.R., Schmidt, P.J., Schneider, R.K., Lord, A.M., Wang, L., Gambe, R.G., et al. (2016). Physiologic expression of Sf3b1(K700E) causes impaired erythropoiesis, aberrant splicing, and sensitivity to therapeutic spliceosome modulation. *Cancer Cell* 30, 404–417.
- Papaemmanuil, E., Gazzola, M., Boultonwood, J., Malcovati, L., Vyas, P., Bowen, D., Pellagatti, A., Wainscoat, J.S., Hellstrom-Lindberg, E., Gambacorti-Passerini, C., et al. (2011). Somatic SF3B1 mutation in myelodysplasia with ring sideroblasts. *N. Engl. J. Med.* 365, 1384–1395.
- Papaemmanuil, E., Gerstung, M., Malcovati, L., Tauro, S., Gundem, G., Van Loo, P., Yoon, C.J., Ellis, P., Wedge, D.C., Pellagatti, A., et al. (2013). Clinical and biological implications of driver mutations in myelodysplastic syndromes. *Blood* 122, 3616–3627, quiz 3699.
- Patnaik, M.M., Lasho, T.L., Finke, C.M., Hanson, C.A., Hodnefield, J.M., Knudson, R.A., Ketterling, R.P., Pardanani, A., and Tefferi, A. (2013). Spliceosome mutations involving SRSF2, SF3B1, and U2AF35 in chronic myelomonocytic leukemia: prevalence, clinical correlates, and prognostic relevance. *Am. J. Hematol.* 88, 201–206.
- Pelossof, R., Fairchild, L., Huang, C.H., Widmer, C., Sreedharan, V.T., Sinha, N., Lai, D.Y., Guan, Y., Premisriut, P.K., Tschaharganeh, D.F., et al. (2017). Prediction of potent shRNAs with a sequential classification algorithm. *Nat. Biotechnol.* 35, 350–353.
- Qian, H., Buza-Vidas, N., Hyland, C.D., Jensen, C.T., Antonchuk, J., Mansson, R., Thoren, L.A., Ekblom, M., Alexander, W.S., and Jacobsen, S.E. (2007). Critical role of thrombopoietin in maintaining adult quiescent hematopoietic stem cells. *Cell Stem Cell* 1, 671–684.
- Robinson, M.D., and Oshlack, A. (2010). A scaling normalization method for differential expression analysis of RNA-seq data. *Genome Biol.* 11, R25.
- Sato, S., Sanjo, H., Takeda, K., Ninomiya-Tsuji, J., Yamamoto, M., Kawai, T., Matsumoto, K., Takeuchi, O., and Akira, S. (2005). Essential function for the kinase TAK1 in innate and adaptive immune responses. *Nat. Immunol.* 6, 1087–1095.
- Shikama, Y., Yamada, M., and Miyashita, T. (2003). Caspase-8 and caspase-10 activate NF-kappaB through RIP, NIK and IKKalpha kinases. *Eur. J. Immunol.* 33, 1998–2006.
- Shu, H.B., Halpin, D.R., and Goeddel, D.V. (1997). Casper is a FADD- and caspase-related inducer of apoptosis. *Immunity* 6, 751–763.
- Starczynowski, D.T. (2014). Errant innate immune signaling in del(5q) MDS. *Blood* 124, 669–671.
- t Hoen, P.A., Hirsch, M., de Meijer, E.J., de Menezes, R.X., van Ommen, G.J., and den Dunnen, J.T. (2011). mRNA degradation controls differentiation state-dependent differences in transcript and splice variant abundance. *Nucleic Acids Res.* 39, 556–566.
- Tang, M., Wei, X., Guo, Y., Breslin, P., Zhang, S., Zhang, S., Wei, W., Xia, Z., Diaz, M., Akira, S., and Zhang, J. (2008). TAK1 is required for the survival of hematopoietic cells and hepatocytes in mice. *J. Exp. Med.* 205, 1611–1619.
- Thol, F., Kade, S., Schlarman, C., Loffeld, P., Morgan, M., Krauter, J., Wlodarski, M.W., Kolking, B., Wichmann, M., Gorlich, K., et al. (2012). Frequency and prognostic impact of mutations in SRSF2, U2AF1, and ZRSR2 in patients with myelodysplastic syndromes. *Blood* 119, 3578–3584.
- Thome, M., Schneider, P., Hofmann, K., Fickenscher, H., Meinl, E., Neipel, F., Mattmann, C., Burns, K., Bodmer, J.L., Schroter, M., et al. (1997). Viral FLICE-inhibitory proteins (FLIPs) prevent apoptosis induced by death receptors. *Nature* 386, 517–521.
- Trapnell, C., Pachter, L., and Salzberg, S.L. (2009). TopHat: discovering splice junctions with RNA-Seq. *Bioinformatics* 25, 1105–1111.
- Varney, M.E., Niederkorn, M., Konno, H., Matsumura, T., Gohda, J., Yoshida, N., Akiyama, T., Christie, S., Fang, J., Miller, D., et al. (2015). Loss of Tifab, a del(5q) MDS gene, alters hematopoiesis through derepression of Toll-like receptor-TRAF6 signaling. *J. Exp. Med.* 212, 1967–1985.
- Vink, P.M., Smout, W.M., Driessen-Engels, L.J., de Bruin, A.M., Delsing, D., Krajnc-Franken, M.A., Jansen, A.J., Rovers, E.F., van Puijenbroek, A.A., Kaptein, A., et al. (2013). In vivo knockdown of TAK1 accelerates bone marrow proliferation/differentiation and induces systemic inflammation. *PLoS One* 8, e57348.

- Wagenmakers, E.J., Lodewyckx, T., Kuriyal, H., and Grasman, R. (2010). Bayesian hypothesis testing for psychologists: a tutorial on the Savage-Dickey method. *Cogn. Psychol.* *60*, 158–189.
- Wang, L., Lawrence, M., Wan, Y., Stojanov, P., Sougnez, C., Stevenson, K., Werner, L., Sivachenko, A., DeLuca, D., Zhang, L., et al. (2011). SF3B1 and other novel cancer genes in chronic lymphocytic leukemia. *N. Engl. J. Med.* *365*, 2497–2506.
- Wei, Y., Dimicoli, S., Bueso-Ramos, C., Chen, R., Yang, H., Neubergh, D., Pierce, S., Jia, Y., Zheng, H., Wang, H., et al. (2013). Toll-like receptor alterations in myelodysplastic syndrome. *Leukemia* *27*, 1832–1840.
- Xin, J., Breslin, P., Wei, W., Li, J., Gutierrez, R., Cannova, J., Ni, A., Ng, G., Schmidt, R., Chen, H., et al. (2017). Necroptosis in spontaneously-mutated hematopoietic cells induces autoimmune bone marrow failure in mice. *Haematologica* *102*, 295–307.
- Xu, Z., Tang, K., Wang, M., Rao, Q., Liu, B., and Wang, J. (2009). A new caspase-8 isoform caspase-8s increased sensitivity to apoptosis in Jurkat cells. *J. Biomed. Biotechnol.* *2009*, 930462.
- Yoshida, K., Sanada, M., Shiraishi, Y., Nowak, D., Nagata, Y., Yamamoto, R., Sato, Y., Sato-Otsubo, A., Kon, A., Nagasaki, M., et al. (2011). Frequent pathway mutations of splicing machinery in myelodysplasia. *Nature* *478*, 64–69.
- Yoshihara, H., Arai, F., Hosokawa, K., Hagiwara, T., Takubo, K., Nakamura, Y., Gomei, Y., Iwasaki, H., Matsuoka, S., Miyamoto, K., et al. (2007). Thrombopoietin/MPL signaling regulates hematopoietic stem cell quiescence and interaction with the osteoblastic niche. *Cell Stem Cell* *1*, 685–697.
- Young, M.D., Wakefield, M.J., Smyth, G.K., and Oshlack, A. (2010). Gene ontology analysis for RNA-seq: accounting for selection bias. *Genome Biol.* *11*, R14.
- Yuan, R.T., Young, S., Liang, J., Schmid, M.C., Mielgo, A., and Stupack, D.G. (2012). Caspase-8 isoform 6 promotes death effector filament formation independent of microtubules. *Apoptosis* *17*, 229–235.
- Zhang, J., Lieu, Y.K., Ali, A.M., Penson, A., Reggio, K.S., Rabadan, R., Raza, A., Mukherjee, S., and Manley, J.L. (2015). Disease-associated mutation in SRSF2 misregulates splicing by altering RNA-binding affinities. *Proc. Natl. Acad. Sci. USA* *112*, E4726–E4734.
- Zhang, S.J., Rampal, R., Manshouri, T., Patel, J., Mensah, N., Kayserian, A., Hricik, T., Heguy, A., Hedvat, C., Gonen, M., et al. (2012). Genetic analysis of patients with leukemic transformation of myeloproliferative neoplasms shows recurrent SRSF2 mutations that are associated with adverse outcome. *Blood* *119*, 4480–4485.
- Zhao, Y., Ling, F., Wang, H.C., and Sun, X.H. (2013). Chronic TLR signaling impairs the long-term repopulating potential of hematopoietic stem cells of wild type but not Id1 deficient mice. *PLoS One* *8*, e55552.
- Zhou, Q., Derti, A., Ruddy, D., Rakiec, D., Kao, I., Lira, M., Gibaja, V., Chan, H., Yang, Y., Min, J., et al. (2015). A chemical genetics approach for the functional assessment of novel cancer genes. *Cancer Res.* *75*, 1949–1958.

STAR★METHODS

KEY RESOURCES TABLE

REAGENT or RESOURCE	SOURCE	IDENTIFIER
Antibodies		
Anti-B220 Alexa Fluor 700 (RA3-6B2)	eBioscience	Cat# 56-0452-82; RRID: AB_891458
Anti-CD19 PECy7 (1D3)	eBioscience	Cat# 25-0193-82; RRID: AB_657663
Anti-CD3 BV605 (17A2)	BioLegend	Cat# 100237; RRID: AB_2562039
Anti-CD4 BV711 (GK1.5)	BioLegend	Cat# 100447; RRID: AB_2564586
Anti-CD8a PerCP/Cy5.5 (53-6.7)	BioLegend	Cat# 100734; RRID: AB_2075238
Anti-Gr-1 PECy7 (RB6-8C5)	eBioscience	Cat# 25-5931-82; RRID: AB_469663
Anti-CD11b/Mac-1 PE (M1/70)	eBioscience	Cat# 12-0112-82; RRID: AB_465546
Anti-NK1.1 APCCy7 (PK136)	BioLegend	Cat# 108724; RRID: AB_830871
Anti-Ter119	BioLegend	Cat# 116223; RRID: AB_2137788
Anti-c-Kit APC (2B8)	eBioscience	Cat# 17-1171-82; RRID: AB_469430
Anti-Sca-1 PECy7 (D7)	eBioscience	Cat# 25-5981-82; RRID: AB_469669
Anti-FcγRIII/III Alexa Fluor 700 (93)	eBioscience	Cat# 56-0161-82; RRID: AB_493994
Anti-CD34 FITC (RAM34)	eBioscience	Cat# 11-0341-82; RRID: AB_465021
Anti-CD45.1 PerCP/Cy5.5 (A20)	BioLegend	Cat# 110728; RRID: AB_893346
Anti-CD45.2 BV605 (104)	BioLegend	Cat# 109841; RRID: AB_2563485
Anti-CD48 PerCP/Cy5.5 (HM48-1)	BioLegend	Cat# 103422; RRID: AB_2075051
Anti-CD150 PE (9D1)	eBioscience	Cat# 12-1501-82; RRID: AB_465873
Anti-CD44 FITC (IM7)	eBioscience	Cat# 11-0441-82; RRID: AB_465045
Anti-IgM PE (II/41)	eBioscience	Cat# 12-5790-82; RRID: AB_465940
Anti-CD25 PE (PC61.5)	eBioscience	Cat # 12-0251-82; RRID: AB_465607
Anti-CD43 FITC (S11)	BioLegend	Cat# 143204; RRID: AB_10960745
Anti-BrdU FITC Flow Kit	BD Pharmingen	Cat# 559619; RRID: AB_2617060
Annexin V FITC Apoptosis Detection Kit	BD Pharmingen	Cat# 556547
Anti-NF-κB/p65 (D14E12)	Cell Signaling Technology	Cat# 8242; RRID: AB_10859369
Anti-phospho NF-κB/p65-Ser536 (93H1)	Cell Signaling Technology	Cat# 3033; RRID: AB_331284
Anti-IκBα, rabbit polyclonal	Cell Signaling Technologies	Cat# 9242; RRID: AB_823540
Anti-TAK1/MAP3K7 (D94D7), rabbit monoclonal	Cell Signaling Technologies	Cat# 5206; RRID: AB_10694079
Anti-Caspase-8, N-terminal (E6), rabbit monoclonal	Abcam	Cat# ab32125; RRID: AB_2068469
Anti-Caspase-8, C-terminal (12F5), mouse monoclonal	Enzo Life Science	Cat# ALX-804-242-C100; RRID: AB_2050949
Anti-β-actin (AC-15), mouse monoclonal	Sigma-Aldrich	Cat# A5441; RRID: AB_476744
Anti-Flag (M2), mouse monoclonal	Sigma-Aldrich	Cat# F1804; RRID: AB_262044
Anti-mouse CD45, rat monoclonal	BD Pharmingen	Cat# 550539; RRID: AB_2174426
Anti-Myeloperoxidase, rabbit polyclonal	Dako	Cat# A0398; RRID: AB_2335676
Anti-Cleaved Caspase-3, rabbit polyclonal	Cell Signaling Technologies	Cat# 9661; RRID: AB_2341188
Anti-mouse Alexa Fluor 488, goat polyclonal	ThermoFisher Scientific	Cat# A-11001; RRID: AB_2534069
Anti-rabbit Alexa Fluor 594, goat polyclonal	ThermoFisher Scientific	Cat# A-11012; RRID: AB_2534079
Prolong Gold Antifade mounting agent	ThermoFisher Scientific	Cat# P36930
Biological Samples		
MDS and CLL primary patient samples	MSKCC	
Chemicals, Peptides, and Recombinant Proteins		
<i>Escherichia coli</i> 0111:B5 LPS	Sigma Aldrich	Cat# L2880
Polybrene	Millipore	Cat# TR-1003-G
Recombinant TRAIL (soluble, human)	Enzo Life Science	Cat# ALX-201-073-3020

(Continued on next page)

Continued

REAGENT or RESOURCE	SOURCE	IDENTIFIER
Recombinant human TNF α	PeproTech	Cat# 300-01A
Recombinant mouse IL-3	R&D	Cat# 403-ML
Recombinant mouse IL-6	R&D	Cat# 406-ML
Recombinant mouse SCF	R&D	Cat# 455-MC
Recombinant mouse TPO	R&D	Cat# 488-TO
Normal goat serum	ThermoFisher Scientific	Cat# PCN500
Actinomycin D	Life Technologies	Cat# 11805-017
Critical Commercial Assays		
MethoCult TM GF M3434	StemCell Technologies	Cat# M3434
NF- κ B Cignal TM Reporter Assay	Qiagen	Cat# CCS-013L
Deposited Data		
RNAseq data	This paper	GSE97452
Experimental Models: Cell Lines		
Human: NALM-6 cells, Parental, <i>SF3B1</i> ^{K700K} , <i>SF3B1</i> ^{K700E} , <i>SF3B1</i> ^{K666N}	Horizon Discovery	Cat# N/A
Human: K562 cells, Parental, <i>SF3B1</i> ^{K700E} , <i>SRSF2</i> ^{P95H}	Horizon Discovery	Cat# N/A
Human: HAP1 Parental cells	Horizon Discovery	Cat# C631
Human: HAP1 <i>CASP8</i> ^{KO} cells	Horizon Discovery	Cat# HZGHC001511c007
Human: 293T cells	ClonTech	Cat# 632180
Human: 293 GPII cells	Clontech	Cat# 631530
Experimental Models: Organisms/Strains		
Mice: <i>Mx1</i> -Cre transgenic mice (C.Cg-Tg(Mx1-cre)1Cgn/J)	The Jackson Laboratory	Cat# JAX: 005673
Mice: <i>Vav</i> -Cre transgenic mice (B6.Cg-Tg(Vav1-cre)A2Kio/J)	The Jackson Laboratory	Cat# JAX: 008610
Mice: <i>Srsf2</i> ^{P95H/+} (B6J.B6NTac(SJL)- <i>Srsf2tm1.1Oaw</i> /J)	Kim et al. 2015	
Mice: <i>Srsf2</i> ^{fl/fl} (B6;129S4- <i>Srsf2tm1Xdfu</i> /J)	The Jackson Laboratory	Cat# JAX: 018019
Mice: <i>Sf3b1</i> ^{K700E/+}	Obeng et al. 2016	
Oligonucleotides		
Please Refer to Table S8		Table S8
Recombinant DNA		
pVSV.G	Addgene	Cat# 12259
psPAX2	Addgene	Cat# 12260
MSCV-IRES-GFP empty vector	Addgene	Cat# 52107
MSCV-Flag-CASP8 ^{FL} -IRES-GFP	This paper	
MSCV-Flag-CASP8 ^{TR} -IRES-GFP	This paper	
MSCV-Flag-mMap3k7-IRES-GFP	This paper	
MSCV-Flag-hMAK3K7-IRES-GFP	This paper	
T3G-dsRED-mirE-PGK-Neo-IRES-rtTA3 (LT3RENIR)	Fellmann et al., 2013	
pMSCV-LTR-mirE-PGK-SV40-IRES-GFP (MLS-E)	Fellmann et al., 2013	
pLKO.Empty Vector-Puro	Kim et al. 2015	
pLKO.sh-UPF1-Puro	Kim et al. 2015	
pNL3.2.NF- κ B-RE Reporter Plasmid	Promega	Cat# N1111
Software and Algorithms		
Bowtie v1.0.0	Langmead et al. 2009	
RSEM v1.2.4	Li and Dewey, 2011	
TopHat v2.0.8b	Trapnell et al. 2009	
TMM method	Robinson and Oshlack 2010	
Wagenmakers's Bayesian framework	Wagenmakers et al. 2010	
MISO v2.0	Katz et al. 2010	

(Continued on next page)

Continued

REAGENT or RESOURCE	SOURCE	IDENTIFIER
GOseq	Young et al. 2010	
Bioconductor	Huber et al. 2015	
Other		
FASTQ files from published RNA-seq studies of patients with MDS	Dolatshad et al. 2015	GSE63569
FASTQ files from published RNA-seq studies of patients with CLL	Darman et al. 2015	GSE72790

CONTACT FOR REAGENT AND RESOURCE SHARING

Further information and requests for resources and reagents should be directed to and will be fulfilled by the Lead Contact, Omar Abdel-Wahab (abdelwao@mskcc.org).

EXPERIMENTAL MODEL AND SUBJECT DETAILS**Animals**

All animals were housed at Memorial Sloan Kettering Cancer Center (MSKCC). All animal procedures were completed in accordance with the Guidelines for the Care and Use of Laboratory Animals and were approved by the Institutional Animal Care and Use Committees at MSKCC. Generation and genotyping of the *Srsf2*^{P95H/+}, *Sf3b1*^{K700E/+} and *Srsf2*^{fl/+} as well as the *Mx1*-Cre and *Vav*-Cre transgenic mice have been previously described (Kim et al., 2015; Obeng et al., 2016). 8-week-old female CD45.1 C57BL/6J mice (The Jackson Laboratory) were used as recipients for bone marrow transplantation assays.

Primary Human MDS and CLL Samples

Studies were approved by the Institutional Review Boards of Memorial Sloan Kettering Cancer Center and conducted in accordance to the Declaration of Helsinki protocol. Patients provided samples after their informed consent and primary human de-identified MDS, AML, and CLL samples derived from whole peripheral blood or BM mononuclear cells were utilized.

Cell Lines

The NALM-6 isogenic cell lines (NALM-6 cells engineered to express the single mutations *SF3B1*^{K700E} or *SF3B1*^{K700K} from the endogenous locus) were cultured in RPMI/10% FCS and K562 isogenic cell lines (engineered to express *SF3B1*^{K700E} or *SRSF2*^{P95H} mutations from each respective endogenous locus) were cultured in IMDM/10% FCS. HAP1 and *CASP8*^{KO} HAP1 cells (obtained from Horizon Discovery) were cultured in IMDM/10% FCS.

METHOD DETAILS**Peripheral Blood Analysis**

Blood was collected by submandibular bleeding using heparinized microhematocrit capillary tubes (Thermo Fisher Scientific). Automated peripheral blood counts were obtained using a ProCyt Dx Hematology Analyzer (IDEXX).

Bone Marrow Transplantation Assays

Primary mouse bone marrow (BM) cells were isolated from *Mx1*-Cre⁺ wild-type (WT), *Mx1*-Cre⁺ *Srsf2*^{P95H/+}, *Mx1*-Cre⁺ *Sf3b1*^{K700E/+}, *Mx1*-Cre⁺ *Srsf2*^{P95H/+} *Sf3b1*^{K700E/+}, *Mx1*-Cre⁺ *Srsf2*^{P95H/P95H} or *Mx1*-Cre⁺ *Srsf2*^{P95H/fl} mice (aged 8 weeks) into cold phosphate-buffered saline (PBS), without Ca²⁺ and Mg²⁺, and supplemented with 2% bovine serum albumin (BSA) to generate single cell suspensions. Red blood cells (RBCs) were removed using ammonium chloride-potassium bicarbonate (ACK) lysis buffer, resuspended in PBS/2% BSA, and filtered through a 40µm cell strainer. Total nucleated cells were quantified by the Vi-Cell XR cell counter (Beckman Coulter). For competitive transplantation experiments, a total of 1.8 x 10⁶ BM cells from donor mice (*Mx1*-Cre⁺ WT, *Mx1*-Cre⁺ *Srsf2*^{P95H/+}, *Mx1*-Cre⁺ *Sf3b1*^{K700E/+}, *Mx1*-Cre⁺ *Srsf2*^{P95H/+} *Sf3b1*^{K700E/+}, *Mx1*-Cre⁺ *Srsf2*^{P95H/P95H}, *Mx1*-Cre⁺ *Srsf2*^{P95H/fl}, *Vav*-Cre⁺ WT, *Vav*-Cre⁺ *Srsf2*^{P95H/+}, and *Vav*-Cre⁺ *Sf3b1*^{K700E/+} CD45.2⁺ mice were mixed with 0.2 x 10⁶ wild-type CD45.1⁺ BM and transplanted via tail vein injection into 8-week old lethally irradiated (2 x 450 cGy) CD45.1⁺ recipient mice. For noncompetitive transplantation experiments, 2 x 10⁶ total BM cells from *Mx1*-Cre⁺ WT, *Mx1*-Cre⁺ *Srsf2*^{P95H/+}, *Mx1*-Cre⁺ *Sf3b1*^{K700E/+}, or *Mx1*-Cre⁺ *Srsf2*^{P95H/+} *Sf3b1*^{K700E/+} mice were injected into lethally irradiated (2 x 450 cGy) CD45.1⁺ recipient mice. To induce the conditional alleles on *Mx1*-Cre background, mice were treated with 3 doses of polyinosinic:polycytidylic acid (pIpC; 12mg/kg/day; GE Healthcare) every other day via intra-peritoneal injection. Peripheral blood chimerism of mature blood cell lineages was assessed routinely by flow cytometry.

In Vivo LPS Stimulation Experiment

For *in vivo* LPS stimulation, *Escherichia coli* 055:B5 LPS (Sigma Aldrich) was used. For chronic LPS exposure, *Vav-Cre*⁺ WT, *Vav-Cre*⁺ *Srsf2*^{P95H/+} and *Vav-Cre*⁺ *Sf3b1*^{K700E/+} received intra-peritoneal injection of LPS (1 mg/kg) every other day for 30 days. For acute LPS exposure, *Mx1-Cre*⁺ WT, *Mx1-Cre*⁺ *Srsf2*^{P95H/+} and *Mx1-Cre*⁺ *Sf3b1*^{K700E/+} mice that have received plpC for 8 weeks prior to activate the mutant alleles were given a single dose of LPS (15 mg/kg) via intra-peritoneal injection.

In Vitro Colony-Forming Assays

Single-cell suspension was prepared from E14.5 fetal livers, and 25,000 cells from each embryo were plated in duplicates in cytokine-supplemented methylcellulose medium (MethoCult™ GF M3434; StemCell Technologies), and colonies were enumerated 10-14 days later. To assess the effect of shRNA-mediated knockdown of target genes, 8-12 week-old C57BL/6 male mice were treated with 5-fluorouracil (150 mg/kg) via intra-peritoneal injection. Five days after injection, BM cells were harvested from the legs (femora and tibiae) and hip bones, and lineage-depletion was performed with biotin-conjugated antibodies against B220 (RA3-6B2), CD19 (1D3), CD3 (17A2), CD4 (GK1.5), CD8a (53-6.7), CD11b (M1/70), Gr-1 (RB6-8C5), NK1.1 (PK136) and Ter119, labeled with anti-biotin MicroBeads (130-090-485; Miltenyi Biotec), and lineage-negative (Lin⁻) cells were magnetically separated using MACS columns according to the manufacturer's instructions. Lin⁻ BM cells were cultured overnight in IMDM/10% FCS supplemented with mIL-3 (10 ng/mL), mIL-6 (10 ng/mL) and mSCF (50 ng/mL). The next day, cells were subjected to spinfection (2,700 rpm for 1 hr) with retroviral supernatants containing shRNAs or cDNAs of interests in the presence of polybrene (5 μg/mL; Millipore). 24 hr after spinfection, cells that were successfully infected with retrovirus were marked with GFP, and were purified by flow cytometry. FACS-sorted cells were cultured in cytokine-supplemented methylcellulose medium (MethoCult™ GF M3434; StemCell Technologies), and colonies were enumerated 10-14 days later.

Flow Cytometry Analyses

Cells were incubated with antibodies in PBS/2% BSA (without Ca²⁺ and Mg²⁺) for 45 min on ice. For hematopoietic stem and progenitor cell analysis from adult mouse bone marrow, cells were stained with a lineage cocktail of monoclonal antibodies including B220 (RA3-6B2), CD19 (1D3), CD3 (17A2), CD4 (GK1.5), CD8a (53-6.7), CD11b (M1/70), Gr-1 (RB6-8C5), NK1.1 (PK136) and Ter119, allowing for mature lineage exclusion from the analysis. For fetal liver analysis, CD11b (M1/70) was excluded from the lineage depletion cocktail. Cells were also stained with antibodies against c-Kit (2B8), Sca-1 (D7), FcγRII/III (93), CD34 (RAM34), CD45.1 (A20), CD45.2 (104), CD48 (HM48-1) and CD150 (9D1). DAPI was used to exclude dead cells. The composition of mature hematopoietic cell lineages in the bone marrow, spleen, thymus and peripheral blood was assessed using a combination of antibodies against B220, CD19, CD3, CD4, CD8a, CD11b, CD25 (PC61.5), CD44 (IM7), Gr-1, IgM (II/41), CD43 (S11). All FACS sorting was performed on FACS Aria, and analysis was performed on an LSR Fortessa (BD Biosciences). Data analysis was performed using the FlowJo software.

Cell Cycle and Apoptosis Analyses

For apoptosis assays, freshly harvested bone marrow or fetal liver cells were first stained with antibodies against cell surface markers of interests, and then stained with FITC-conjugated Annexin-V in Annexin-V binding buffer (BD Pharmingen) according to manufacturer instructions. For assessment of cell cycle status in adult bone marrow HSPCs, BrdU (1 mg/kg) was administered via intra-peritoneal injection to adult mice 48 hr prior to sacrifice. For cell cycle analysis of E14.5 fetal HSPCs, BrdU (1 mg/kg) was administered to pregnant mice via intra-peritoneal injection 3 hr prior to harvesting fetal livers. Assessment of BrdU incorporation was performed following manufacturer instructions (BD Pharmingen) and data was acquired on a LSR Fortessa (BD Biosciences).

Histological Analysis

Tissues, embryos and pups were fixed in 4% paraformaldehyde, processed routinely in alcohol and xylene, embedded in paraffin, sectioned at 5-micron thickness, and stained with hematoxylin-eosin (H&E). Multiple sections were obtained through the head in the coronal plane, trunk in the transverse plane, and fore and hind limbs in the longitudinal plane. Immunohistochemistry (IHC) was performed on a Leica Bond RX automated stainer (Leica Biosystems, Buffalo Grove, IL). Following HIER at pH 6.0, the primary antibody against mouse CD45 (BD Pharmingen; 550539), myeloperoxidase (Dako; A0398), and cleaved caspase-3 (Cell Signaling; 9661) were applied at a concentration of 1:250, 1:1000, and 1:250 respectively, followed by application of a polymer detection system (DS9800, Novocastra Bond Polymer Refine Detection, Leica Biosystems) in which the chromogen was 3,3-diaminobenzidine tetrachloride (DAB) and counterstain was hematoxylin. For quantification of cleaved caspase-3 by image analysis, whole slide digital images were generated on a slide scanner (Pannoramic 250 Flash III, 3DHitech, 20x/0.8NA objective, Budapest, Hungary) at a resolution of 0.2431 μm per pixel. Staining quantification was performed with QuPath 0.1.2 software (Centre for Cancer Research & Cell Biology, Queen's University Belfast, UK). The region of interest (ROI) was defined as the liver parenchyma. The number of DAB positive cells per mm² was measured with the positive cell detection algorithm. ROI selection and algorithm optimization and validation, and qualitative examination of all H&E and IHC slides were performed by a board-certified veterinary pathologist (S.M.).

Immunoblot

For immunoblotting, the following antibodies were used: NF- κ B/p65 (CST; 8242), phosphorylated NF- κ B/p65-Ser536 (CST; 3033), I κ B- α (CST; 9242), TAK1/MAP3K7 (CST; 5206), Caspase-8, N-terminal (Abcam; clone E6), Caspase-8, C-terminal (Enzo Life Science; clone 12F5), Flag (Sigma-Aldrich; F-1804), β -actin (Sigma-Aldrich; A-5441).

Immunofluorescence

Following stimulation with LPS (Sigma-Aldrich), TNF α (PeproTech), or TRAIL (Enzo Life Science), cells were fixed with 4% paraformaldehyde/PBS for 10 min at room temperature (RT), permeabilized with PBS-T (PBS/1% BSA/0.2% Triton-X) for 15 min, blocked with PBS-T/5% goat serum (ThermoFisher PCN500) for 1 hr at RT, and incubated with primary antibodies (1:50 dilution for p-p65 and 1:100 for Flag) in PBS-T/5% goat serum overnight at 4°C. Cells were washed three times with PBS-T for 10 minutes at RT with gentle agitation, and were incubated with goat anti-rabbit Alexa Fluor 594 (ThermoFisher Scientific; A-11012) or goat anti-mouse Alexa Fluor 488 (ThermoFisher Scientific; A-11001) secondary antibodies (1:500 dilution in PBS-T/5% normal goat serum) for 2 hr at RT in the dark. Cells were then washed twice with PBS-T for 10 min at RT, and counter-stained with DAPI (0.5 μ g/mL; Sigma-Aldrich; D-9542) for 20 min at RT. Cells were coverslipped with ProLong Gold anti-fade (ThermoFisher Scientific; P36930). Images were captured using either a confocal microscope (Leica TCS SP5, Upright; Leica Microsystems), or were digitally scanned with a Panoramic Confocal Scanner (3DHitech, Budapest Hungary) using a 20x/0.8NA objective. The projected images were exported into tif format using CaseViewer software (3DHitech) and analyzed with ImageJ/FIJI. A macro was written that segments each nucleus using the DAPI channel and measures the p-p65 intensity within the nucleus after appropriate threshold was set.

Caspase-8 and MAP3K7 Constructs

MSCV-Flag-CASP8^{FL}-IRES-GFP, MSCV-Flag-CASP8^{TR}-IRES-GFP, MSCV-Flag-MAK3K7-IRES-GFP (human), MSCV-Flag-Map3k7-IRES-GFP (mouse) and MSCV-IRES-GFP empty vector constructs were used for overexpression studies. Retroviral supernatants were produced by transfecting 293 GP11 cells with cDNA constructs and the packaging plasmid VSV.G using XtremeGene9 (Roche), and were used to transduce HAP1, CASP8^{KO} HAP1 and K562 parental and SF3B1^{K700E} isogenic cells in the presence of polybrene (5 μ g/mL; Millipore). Successfully transduced cells expressing GFP were purified by flow cytometry. Cells were stimulated with LPS (Sigma-Aldrich), TNF α (PeproTech) or TRAIL (Enzo Life Science).

mRNA Stability Assay

For mRNA half-life measurement using qRT-PCR, UPF1 shRNA and control lentivirus infected K562 SF3B1^{K700E} cells were treated with 2.5 μ g/ml Actinomycin D (Life Technologies) and harvested at 0, 2, 4, 6, and 8 hr (following protocols established previously (t Hoen et al., 2011)). MAP3K7 inclusion, MAP3K7 exclusion and 18s rRNA mRNA levels were measured by qRT-PCR.

Luciferase Reporter Assay

We generated K562, NALM-6 SF3B1 isogenic cells, HAP1 and CASP8^{KO} HAP1 cells expressing the luciferase reporter for NF- κ B response elements by following the manufacturer instructions (SignalTM Reporter Assay, Qiagen). Cells were stimulated with LPS, TNF α or TRAIL as described above, and NF- κ B activity was assessed by luciferase intensity using the Dual-Luciferase Reporter Assay System (Promega) according to the manufacturer instructions. To verify that the luciferase reporter assay was not aberrantly activated by basal leakiness, we used another NF- κ B reporter plasmids (Promega; N1111) with known NF- κ B response elements (RE), and performed mutagenesis in the NF- κ B-RE using the QuiKChange II Site-Directed Mutagenesis Kit (Agilent Technologies; #200522). There are five putative NF- κ B-RE binding sites in this reporter plasmid (5'-GGGRNTTCC-3', where R is a purine, Y is a pyrimidine and N is any nucleotide). To mutagenize the binding sequence, the "TTTC" sequence was mutated to "AAAA". The primers used to create the two mutant plasmids are:

Mutant-Fwd

GGTACCTGAGCTCGCTAGCGGGAAAAAACGGGGACAAAACGGGAAAAAACGGGGACAAAACGGGAAAAAACAGATCTGGCCTC
GGCGCCAAGCTTA.

Mutant-Rev

TAAGCTTGGCCCGGAGGCCAGATCTGTTTTTCCCCTTTTGTCCCGTTTTTCCCCTTTTGTCCCGTTTTTCCCCTAGCGAG
CTCAGGTACC.

RT-PCR and Quantitative RT-PCR (qRT-PCR)

Total RNA was isolated using RNeasy Mini kit (Qiagen). For cDNA synthesis, total RNA was reverse transcribed to cDNA with SuperScript VILO cDNA synthesis kit (Life Technologies). The resulting cDNA was diluted 10-20 fold prior to use. Quantitative RT-PCR (qRT-PCR) was performed in 10 μ L reactions with either SYBR Green PCR Master Mix or Taqman Gene Expression Master Mix with AmpErase (ThermoFisher Scientific). All qRT-PCR analysis was performed on an Applied Biosystems QuantStudio 6 Flex Cycler (ThermoFisher Scientific). Relative gene expression levels were calculated using the comparative CT method.

Primers used in RT-PCR reactions were:

MAP3K7 (human) – Fwd: GATGGAATATGCTGAAGGGG, Rev: CACTCCTTGGGAACACTGTA

Map3k7 (mouse) – Fwd: GATGGAATATGCAGAGGGG, Rev: CACTCCTTGGGAACACTGTA

CASP8 (human) – Fwd: GAACTTCAGACACCAGGC, Rev: CTTTGTCCAAAGTCTTTGCTG

Primers used in qRT-PCR reactions were:

CASP8 exclusion isoform (aberrant):

Fwd: GATGAATTTTCAAATGACTTTGGAC

Rev: TGATCAGACAGTATCCCCGAG

CASP8 inclusion isoform (canonical):

Fwd: TGATGAATTTTCAAATGGGGAGGA

Rev: ATCCTGTTCTCTTGGAGAGTCC

MAP3K7 mRNA half-life experiment (human):

Fwd (common): GCGTTTATTGTAGAGCTTCGG

Rev (canonical): GCACCATGCAGCACATTATATAAAG

Rev (aberrant): CATGCAGCACTGCGAAAGAAAG

Taqman probes were used for gene expression analysis of TNF (Hs00174128_m1), IL-1 β (Hs01555410_m1), GAPDH (Hs02786624_g1), Mpl (Mm00440310_m1), Pbx1 (Mm04207617_m1), Itga2b (Mm00439741_m1), and Hprt (Mm03024075_m1).

shRNA Experiments

NALM-6 parental cells carrying the NF- κ B luciferase reporter were transduced with a doxycycline-inducible lentiviral vector, T3G-dsRED-mirE-PGK-Neo-IRES-rtTA3 (Fellmann et al., 2013), expressing shRNAs for MAP3K7 or a non-targeting renilla or firefly luciferase control. Transduced cells were selected with G418 (0.5 mg/mL; ThermoFisher Scientific), and the short hairpins were induced with the addition of doxycycline (2.0 μ g/mL; Sigma Aldrich). All mouse shRNAs used in clonogenic assays were cloned into the retroviral pMSCV-LTR-mirE-PGK-SV40-IRES-GFP (MLS-E) backbone (Fellmann et al., 2013). All shRNAs were designed using the SplashRNA algorithm (Pelossof et al., 2017). The short hairpin sequences are:

sh-MAP3K7.748: TTAGGTAAATTTTTATCAGTG

sh-MAP3K7.1041: TTTTCAACAATTTTGATTCTAA

sh-Luciferase control: TTAATCAGAGACTTCAGGCGGT

sh-Ren.713 control: CAGGAATTATAATGCTTATCTA

sh-Mpl.2121: TTATATAATAAACAGTGTCTAA

sh-Mpl.2368: TCAAATAAATAGATGACAGCAA

sh-Pbx1.824: TTCATCCAAACTCTGGTCTGTG

sh-Pbx1.1393: TCATTCAGAATTTCTGTGGCTT

sh-Itga2b.2279: TTCTCTTCTTCTGAGTGCAGA

sh-Itga2b.3380: TTAGGAAAAGGGATGCACCCGG

sh-UPF1 (TRCN0000022254): CCGGGCATCTTATTCTGGGTAATAACTCGAGTTATTACCCAGAATAAGATGCTTTTT

mRNA Isolation, Sequencing, and Analysis

RNA was extracted from sorted mouse cell populations using Qiagen RNeasy columns. Poly(A)-selected, unstranded Illumina libraries were prepared with a modified TruSeq protocol. 0.5X AMPure XP beads were added to the sample library to select for fragments <400 bp, followed by 1X beads to select for fragments >100 bp. These fragments were then amplified with PCR (15 cycles) and separated by gel electrophoresis (2% agarose). 300 bp DNA fragments were isolated and sequenced on the Illumina HiSeq 2000 (~100M 101 bp reads per sample).

Genome Annotations

Genome annotations for the human (NCBI GRCh37/UCSC hg19) and mouse (NCBI GRCm38/UCSC mm10) genomes were created as previously described (Dvinge et al., 2014). Genome annotations from the Ensembl (Flicek et al., 2013) and UCSC (Meyer et al., 2013) databases were merged with splicing event annotations from MISO v2.0 (Katz et al., 2010). An additional annotation of all possible combinations of annotated 5' and 3' splice sites found in the merged annotation was created for read mapping. Constitutive introns were defined as those whose associated 5' and 3' splice sites were alternatively spliced in the UCSC annotation.

RNA-seq Read Mapping

RNA-seq reads were sequentially mapped to the transcriptome and genome as previously described (Dvinge et al., 2014). Reads were first mapped to the transcriptome using Bowtie v1.0.0 (Langmead et al., 2009) and RSEM v1.2.4 (Li and Dewey, 2011). The resulting read alignments were then filtered to require that reads spanning splice junctions overlapped the flanking exons by at least six nt. The remaining unaligned reads were then mapped to the genome and splice junctions using TopHat v2.0.8b (Trapnell et al., 2009), where reads were only allowed to align to the splice junctions present in the file of all possible combinations of annotated 5' and 3' splice sites described above. The resulting read alignments were then merged with the output of RSEM's alignment to create a final file of aligned reads.

Differential Gene Expression Analysis

Gene expression analysis was performed using the gene expression estimates computed by RSEM in units of transcripts per million (TPM). Those estimates were then further normalized using the TMM method (Robinson and Oshlack, 2010), with a reference set of all protein-coding genes. Differentially expressed genes were defined as those with an associated Bayes factor ≥ 100 (computed using Wagenmakers's Bayesian framework (Wagenmakers et al., 2010)) and an associated fold-change ≥ 1.5 .

Differential Splicing Analysis

Isoform ratios for annotated splicing events (cassette exons, competing 5' and 3' splice sites, and annotated retained introns) were calculated using MISO v2.0 (Katz et al., 2010). Splicing of constitutively spliced introns and junctions was quantified using only junction-spanning reads, as previously described (Hubert et al., 2013). Differential splicing in the murine data was identified by comparing samples from different genotypes for a single replicate in a pairwise fashion. The analysis was restricted to splicing events with at least 20 informative reads, where an informative read is defined as a read that distinguishes between isoforms. Differentially spliced events were defined as those with an associated Bayes factor was ≥ 5 (computed using Wagenmakers's Bayesian framework (Wagenmakers et al., 2010)) and absolute change in isoform ratio of $\geq 10\%$. Differential splicing in the human patient cohorts was identified using a group statistical test to identify differences between patient samples with or without defined splicing factor mutations. Differentially spliced events were defined as those with an associated p value ≤ 0.05 (computed using the Wilcoxon rank-sum test) and an absolute change in median per-group isoform ratio of $\geq 10\%$.

Gene Ontology (GO) Enrichment Analysis

GO enrichment analysis was performed using the GSeq method (Young et al., 2010) to correct for sequencing depth biases. The background set of genes was defined as all protein-coding genes. False discovery rates were calculated using the Wallenius method and corrected using the Benjamini-Hochberg method. We restricted reporting of enriched terms to those with at least two ancestors and fewer than 500 associated genes.

Motif Enrichment Analysis and Sequence Logos

The relative enrichment of different ESEs was computed by comparing motif occurrence within and adjacent to cassette exons that were promoted versus repressed in cells or samples with versus without defined splicing factor mutations. These analyses were performed using all cassette exons that were differentially spliced in at least one mouse replicate for a given genotype comparison. 95% confidence intervals were calculated by bootstrapping with 500 resampling steps. Sequence logos centered on intron-proximal or intron-distal 3' splice sites were created using all competing 3' splice sites that were differentially spliced in at least one mouse replicate for a given genotype comparison. The analysis was restricted to events with canonical GT and AG dinucleotides at the 5' and 3' splice sites. These analyses relied upon the GenomicRanges package in Bioconductor (Huber et al., 2015).

Analysis of Expected and Observed Gene Expression Convergence

Expected gene expression programs for *Mx1-Cre⁺ Srsf2^{P95H/+} Sf3b1^{K700E/+}* samples were calculated by computing the mean of individual gene expression levels between *Mx1-Cre⁺ Srsf2^{P95H/+}* and *Mx1-Cre⁺ Sf3b1^{K700E/+}* samples for each replicate. This method of computing the expected gene expression program was motivated by the assumption that mutations in *Srsf2* and *Sf3b1* have independent consequences for individual gene expression. Gene dysregulation for the expected gene expression program was then calculated as described previously for the actual, observed gene expression values.

The numbers of dysregulated genes that were convergent between the expected gene expression program and the two *Mx1-Cre⁺ Srsf2^{P95H/+}* and *Mx1-Cre⁺ Sf3b1^{K700E/+}* single mutants was then determined for each replicate, again using a method identical to that for the actual, observed gene expression values (Figure S4A). A one-sided binomial proportion test was then used to test whether there were more dysregulated genes that were observed than expected (Figure S4B).

QUANTIFICATION AND STATISTICAL ANALYSIS

Statistical Analyses

All data are presented as mean \pm standard deviation, unless otherwise stated. The replicate for each experiment was stated in the figure legend or indicated in the figure. Statistical significance was determined by analysis of variance (ANOVA) after testing for normal distribution and equal variance, followed by Tukey's post-hoc test for multiple group comparisons. A p value of <0.05 was considered statistically significant. For non-normally distributed data, a non-parametric test (Kruskal-Wallis) was used, followed by multiple group comparisons using false-discovery rate (FDR). For Kaplan Meier survival analysis, Mantel-Cox log-ranked test was used to determine statistical significance. For offspring frequency analysis, a Chi-Square test was performed to test the difference between observed and expected frequencies from different genotypes. No blinding or randomization was used. Unless otherwise noted, all immunoblot quantitation and immunofluorescence image quantitation were representative of at least three biological replicates from independent experiments. Data were plotted using GraphPad Prism 7 software.

DATA AND SOFTWARE AVAILABILITY

Publicly Available RNA-seq Data

FASTQ files from published RNA-seq studies of patients with MDS ([Dolatshad et al., 2015](#)) and CLL ([Darman et al., 2015](#)) were downloaded from GEO series GSE63569 and GSE72790.

Accession Codes

Gene Expression Omnibus: The accession number for all newly generated RNA-seq data reported in this paper are deposited into the GEO database (accession number GSE97452).